Functional Scanning Ion Conductance Microscopy

Ashley Page,[1,2] David Perry[1,2] and Patrick R. Unwin[1,]*

[1]Department of Chemistry and [2]MOAC Doctoral Training Centre, University of Warwick, Coventry, CV4 7AL, United Kingdom

*p.r.unwin@warwick.ac.uk

Abstract

Scanning ion conductance microscopy (SICM) is a nanopipette-based technique that has traditionally been used to image topography or to deliver species to an interface, particularly in a biological setting. This article highlights the recent blossoming of SICM into a technique with a much greater diversity of applications and capability that can be probed either standalone, with the use of advanced control (potential-time) functions, or in tandem with other methods. SICM can be used to elucidate functional information about interfaces, such as surface charge density or electrochemical activity (ion fluxes). Using a multi-barrel probe format, SICM-related techniques can be used to deposit nanoscale 3D structures and further functionality is realised when SICM is combined with scanning electrochemical microscopy (SECM), with simultaneous measurements from a single probe opening up considerable prospects for multifunctional imaging. SICM studies are greatly enhanced by finite element method modelling for quantitative analysis to treat issues such as resolution, surface charge and (tip) geometry effects. SICM is particularly applicable to the study of living systems, such as single cells, although applications extend to materials characterisation and to new methods of printing and nanofabrication. A more thorough understanding of the electrochemical principles and properties of SICM provides a foundation for significant applications of SICM in electrochemistry and interfacial science.

Keywords

Scanning ion conductance microscopy, nanopipette, electrochemical imaging, cellular imaging, single cell analysis, charge mapping.

1. INTRODUCTION

This article is concerned with scanning ion conductance microscopy (SICM), a scanning probe microscopy (SPM) technique first introduced in 1989 by Hansma [1]. We will show, in particular, how its capabilities can be advanced and its function extended to applications beyond topographical mapping, for which it has traditionally been used [2–4]. Recent developments have provided a much better understanding of the instrument response, and new methods are being developed that make increasing use of the electrochemical (potential-control) functions. A further trend has been the combination of SICM with other SPMs and with spectroscopic and wide-field microscopy methods.

SPM techniques encompass a diverse family of microscopic tools that involve using a physical probe to obtain information and/or images of substrates and interfaces [5]. Each SPM technique takes advantage of a specific type of interaction between a probe (or tip) and an interface in order to provide morphological or functional information on the interface. Primary examples of SPM techniques include atomic force microscopy (AFM) [6,7] and scanning tunnelling microscopy (STM) [8,9]. Scanning electrochemical microscopy (SECM) [10,11] and scanning ion conductance microscopy (SICM) [1,4] represent prominent techniques where the probe is under electrochemical control. Electrochemical probes offer interesting applications for mapping and manipulating interfacial fluxes [12–16].

Hitherto, SECM has been used much more extensively than SICM, with a diversity of applications concerning the redox activity of electrodes and for measuring chemical fluxes at other interfaces [17–21], as well as for detection of various ions and pH using functionalised electrodes [22–25]. However, a longstanding drawback of SECM is that the probe response depends on both substrate topography (separation

between the tip and surface) and activity, and separating these effects from the electrochemical signal has proved to be non-trivial [19,26]. Additionally, nanoscale SECM probes, needed for high spatial resolution measurements, are rather difficult to fabricate, handle and characterize [27]. Hybrid techniques such as SICM-SECM [28–32], which we discuss herein, as well as AFM-SECM [33–36], shear force SECM [37] and intermittent contact SECM [38] neatly solve the topography-activity conundrum by introducing an independent means of sensing the distance between a functional probe and surface and enhance the prospects of making topography-activity maps of a surface with a single electrochemical probe.

In contrast to SECM, SICM uses a much simpler type of probe and employs feedback (distance) control, but has mainly been used for topographical imaging. The purpose of this review is to discuss the recent emergence of SICM as a powerful multifunctional technique, with significant life science applications, but also with scope in other areas such as in materials research, including patterning and printing [39]. To place recent work in context, we briefly review the use of SICM as a topographical tool, before a comprehensive examination of how the SICM response is affected by a multitude of surface and bulk phenomena. This leads to new uses, in which careful interpretation of the SICM signal opens up avenues to map a number of surface properties, along with topography, as exemplified through studies of interfacial charge and reactivity [40–44]. Multi-channel probes provide further means of combining SICM with other SPMs and the SICM platform is readily combined with optical techniques. These advances lead to growing prospects for SICM as a tool for probing and imaging biological function, and for nanoscale studies in electrochemistry and interfacial science, where ion fluxes and interfacial charge are of paramount importance. This review mainly focuses on recent work from our group,

and includes unpublished data as well as material from published papers, but we also reference other studies, as appropriate.

2. BACKGROUND

2.1 Principles of Operation

SICM is mainly used for probing interfaces that are bathed in an ionically-conducting solution. In a typical setup, a single channel nanopipette probe, pulled from a glass or quartz tube, is filled with an electrolyte solution and a quasi-reference counter electrode (QRCE) is inserted, with a second QRCE placed in bulk solution. A bias is applied between the two QRCEs to drive an ionic current through the end of the nanopipette, as shown in Figure 1a. In bulk solution, with the probe positioned away from the substrate, the resistance of the nanopipette, together with that of the electrolyte solution, mainly determine the magnitude of the ionic current that flows. The majority of the current-limiting resistance is attributed to the narrowest region of the nanopipette near the opening. As the inner lumen of the pipette increases, the contribution to the overall pipette resistance decreases [4].

As the nanopipette is brought towards a substrate of interest, the conventional view [1,4] has been that the ionic current decreases, most noticeably when the probe-substrate distance is less than one tip diameter. At these separation distances, the increased access resistance, caused by the narrowing gap between the pipette walls and the substrate, becomes comparable to the nanopipette resistance. Consequently, the overall system resistance increases, as shown in Figure 1b, resulting in an observable decrease in the ionic current flowing through the pipette, as depicted in Figure 1c. With this simple model, the SICM response can be modelled in terms of a series of resistors, and Ohm's Law applies [45,46]. This predictable response occurs

under a range of imaging conditions and the drop in the ionic current provides a means by which the probe can sense a surface of interest. By extracting the position of the nanopipette at the point of closest approach at an array of pixels across a surface, topographical maps such as that seen in Figure 1d can be constructed. It has recently been shown, however, that under certain conditions, for example, on approach to charged interfaces in lower ionic strength solutions, and/or with smaller tips, the SICM response is also influenced by the electrical double layer (EDL) at the substrate. Indeed, as we describe herein, depending on the tip polarity and substrate surface charge, the current may actually increase as the tip-substrate separation decreases [40,41]. These charge effects must be carefully considered when using SICM for topographical imaging [40–42,47]. We discuss this aspect of SICM and a new SICM methodology (tuneable potential control), that opens up charge mapping with SICM, while removing charge effects in topographical imaging (section 5).

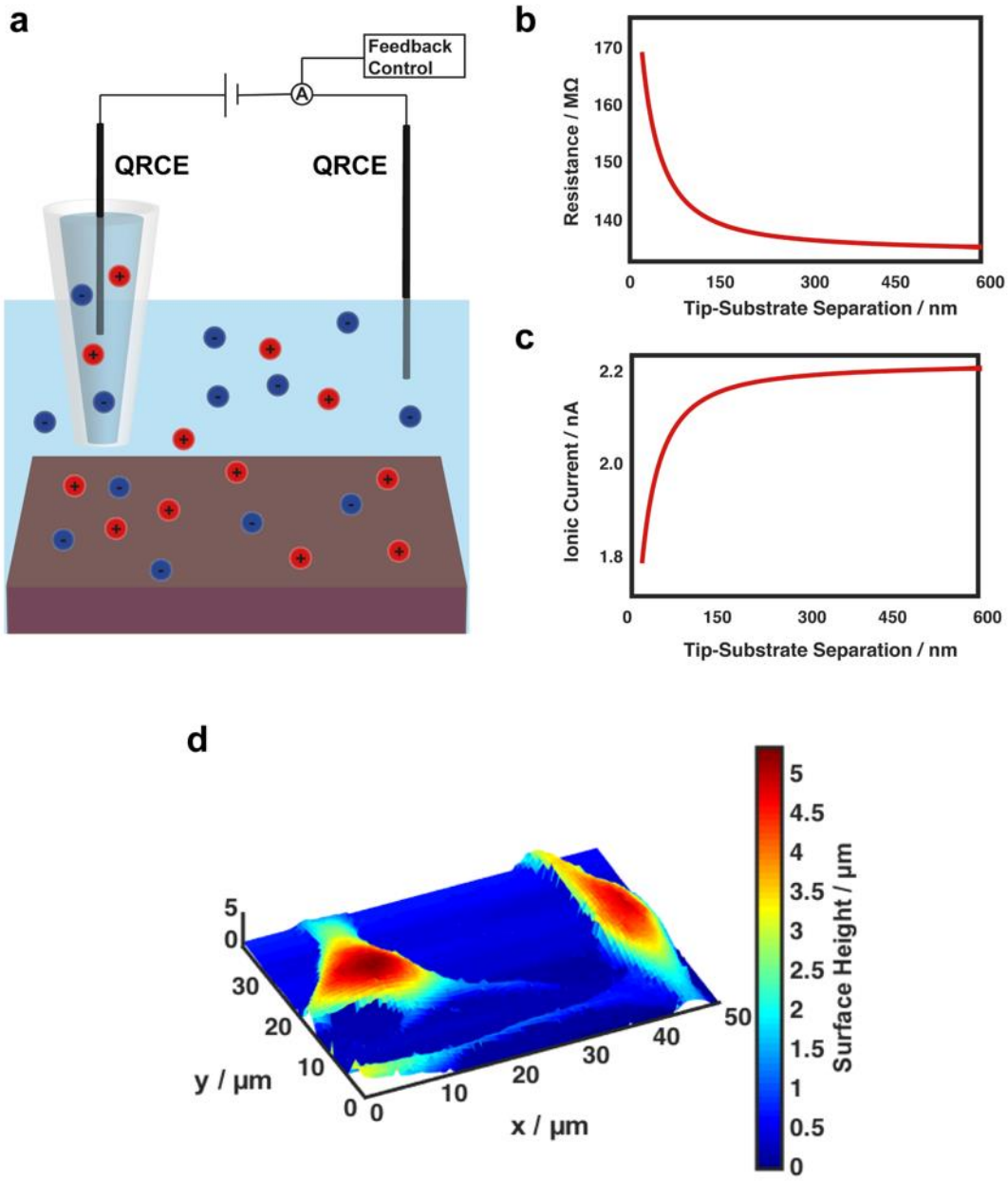

Figure 1. a) Schematic of the SICM setup with a nanopipette filled and bathed in electrolyte solution above a substrate of interest. A bias is applied between a QRCE in the nanopipette and one in bulk solution in order to generate an ionic current that can be used as a means of the nanopipette sensing the surface. **b)** Simulated resistance approach curve of a nanopipette, with 100 nm diameter, approaching an uncharged surface at 300 mV tip bias in 10 mM KCl. Upon approaching within about one tip

diameter of the surface, an increase in the resistance is observed due to the reduced access of ions to the probe opening. **c)** Corresponding ionic current as a function of tip-substrate distance from the simulation in **(b)**. **d)** Topographical image of three PC12 cells, with surface heights extracted from the point of closest approach at each pixel (hopping mode scan regime).

2.2 Scanning Regimes and Feedback types

When close to a surface, the probe can be moved laterally in one of two regimes. In the constant-distance mode (Figure 2a), the probe is moved across the surface while the piezo positioners adjust the position of the nanopipette to maintain a constant current value, corresponding to a constant probe-separation distance, similar to constant-distance STM [8], although the principles underlying the current generation are obviously very different. Constant-distance scanning is usually performed in a raster scan pattern [1,2,4,48], where line-by-line maps are generated, with a typical scan profile shown in Figure 2b. More recently, a spiral scan profile has been introduced into SICM experiments [43,49], also depicted in Figure 2b, greatly increasing image acquisition rates. In this configuration, the piezo positioners used to control the nanopipette (or sample) movement in the *x*-*y* plane are moving continuously. In section 5 we discuss how this approach can be implemented into a routine for dynamic electrochemical reaction mapping.

Alternatively, pixel-wise measurements can be performed whereby, once the set point current value is reached, upon vertical approach of the probe to the surface (*z* direction), the probe is retracted and moved laterally to a new location before repeating the same approach (Figure 2c). This has advantages for mapping samples with large height gradients, which would be difficult to track with a constant-distance

scan mode. This scan regime is known as a "hopping" or "standing-approach" mode [50–52]. Whilst the constant-distance mode enables faster scanning, an interesting feature of hopping mode is that it allows "self-referencing" measurements as the response in bulk and near the surface can be compared at each pixel. This becomes particularly beneficial when using SICM to elucidate surface properties other than topography, or if the probe response changes (e.g. the signal drifts) over the relatively long times that can be required to acquire images. Moreover, this mode allows simpler, but robust modelling and analysis of the current response. Each of these scan profiles can be used in combination with different types of feedback, which are now discussed.

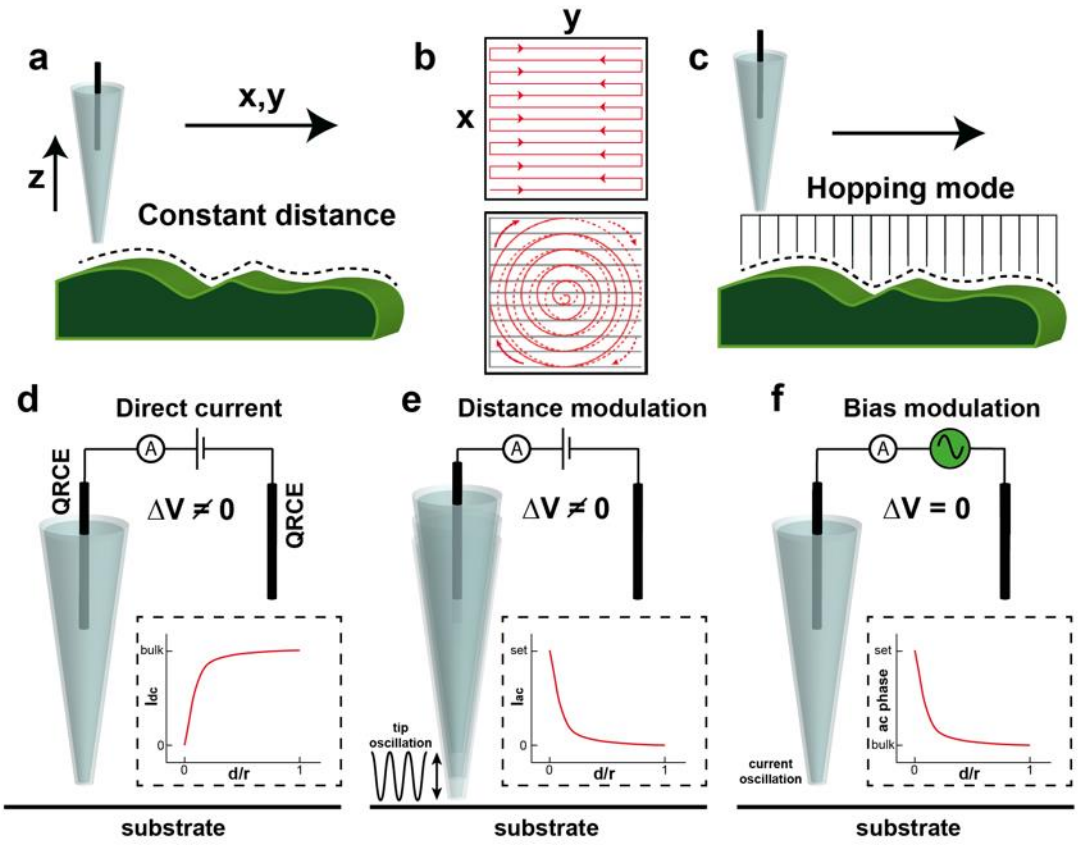

Figure 2. The SICM probe is typically employed in one of two scanning regimes, either with a fixed probe-substrate separation in constant-distance mode **(a)** with a raster or spiral scan profile **(b)** or by hopping across the surface **(c)**. Schematic

depiction of three SICM feedback types. In the DC approach **(d)**, a decrease in the ionic current is usually used to sense the substrate. In DM-SICM **(e)**, an oscillation is applied to the *z*-piezoelectric positioner controlling the tip, generating an AC current between the two QRCEs, the magnitude of which is only significant when the nanopipette approaches the substrate. In BM-SICM **(f)**, an oscillation is applied to the bias between the QRCE in the nanopipette and that in bulk solution, generating an AC signal, which is sensitive to the substrate even when zero net bias is applied between the QRCEs. **d-f**) are adapted with permission from Reference 12. Copyright 2016 American Chemical Society.

The use of the ionic current as a means of feedback for topographical mapping is often termed direct current (DC) feedback (Figure 2d) in SICM experiments [4]. However, the ionic current may sometimes be susceptible to drift, which is problematic in constant-distance imaging. To overcome this problem, modulation techniques can be employed to generate an AC signal between the QRCEs. Oscillation of the nanopipette position normal to the surface at an applied frequency, typically in the 100 Hz - 1000 Hz range (Figure 2e), results in an ionic current response at the same frequency that can be measured with a lock-in amplifier, which also provides the harmonic potential signal for the modulation of the z-piezoelectric positioner. The AC amplitude and/or phase is much more stable [53–56] and more sensitive to nanopipette position near the surface.

Using this approach, when the nanopipette is in bulk solution, typically more than one tip diameter away from the surface [4], the AC signal is small because there is little difference in the resistive state at the furthest and closest points of the probe-surface distance during the oscillation (Figure 2e). However, at closer distances, there

is a noticeable change in resistance during the oscillation period and, as such, there will be an AC signal that can be picked out with the lock-in amplifier. Typically, in distance modulated (DM-) SICM experiments, a value of the AC amplitude is set and used for feedback (Figure 2e) [55,57], with a z-piezoelectric positioner adjusting to maintain this value and hence trace substrate topography [4].

An alternative modulation method, known as bias modulation (BM-) SICM (Figure 2f) has recently been developed by our group, whereby an AC signal is generated by oscillating the bias between the two QRCEs with a small amplitude [58]. This approach has several advantages over the DM-SICM scheme; most significantly that it is possible to operate with no net bias applied. As discussed in section 5, this renders the SICM response essentially insensitive to surface charge, when desired, making SICM a truer tool for topographical mapping [41]. Moreover, there are concerns over operating SICM with a strong bias for topographical imaging of cells due to the intense electric field at the end of the tip [42]. BM-SICM greatly reduces such effects.

BM-SICM measurements provide single frequency impedance data. Typically, the SICM response to an uncharged interface is represented by an equivalent circuit diagram, such as that in Figure 3a. Upon approach to an uncharged interface, the access resistance increases. In BM-SICM measurements, this increase in resistance is manifested as an increase in the phase component of the AC signal and a decrease in AC amplitude (Figure 3b). As the resistance increases, a higher proportion of the current flows through the capacitive part of the system, resulting in the phase tending to 90 degrees with respect to the applied alternating bias. This change in the AC response - phase or amplitude - can be used as a feedback signal for probe positioning. Impedance measurements (Figure 3c) performed with a 150 nm diameter

nanopipette in bulk solution, and near a glass interface, in 100 mM KCl, show an increase in the impedance as the tip-substrate distance decreases.

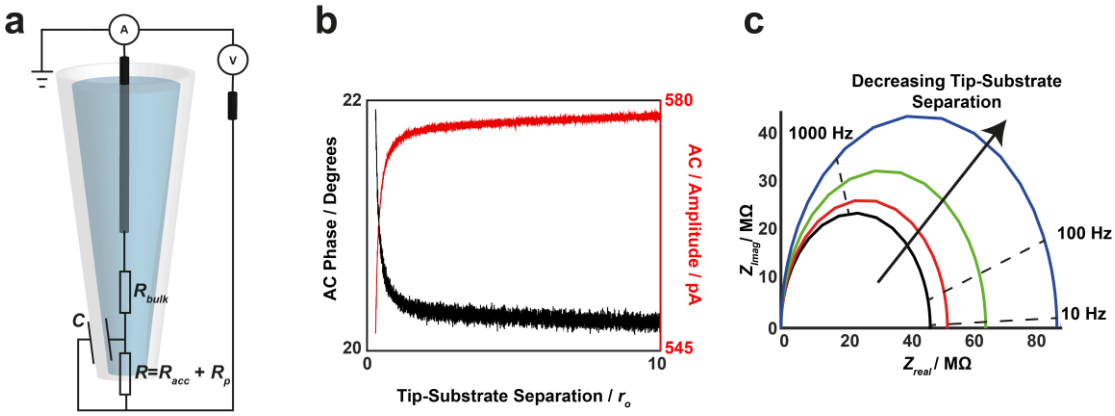

Figure 3. a) Typical equivalent circuit diagram to explain the BM-SICM response, where R_{bulk}, R_{acc} and R_p represent the resistance of the bulk solution, the access resistance and the probe resistance respectively, while C is the capacitance across the wall of the pipette. **b)** Experimental approach curves (tip current response as a function of tip-radius-normalised distance between the tip and surface) of a 75 nm radius (r_o) borosilicate glass nanopipette to a glass surface at 0 V net bias in 100 mM KCl solution (10 mV modulation amplitude and 270 Hz frequency), showing the change in AC phase and amplitude with tip-substrate separation. **c)** BM-SICM impedance data of the system in **(b)** with the nanopipette in bulk (black line), and at tip-substrate distances of approximately 150 nm (red line), 100 nm (green line) and 50 nm (blue line). Upon approach to an interface with no net bias, the impedance can be seen to increase.

Figure 4 shows example topographical maps, obtained using BM-SICM to highlight the range of possible substrates that can be imaged, including polymer films (Figure 4a), living cells (Figure 4b) and electrode surfaces (Figure 4c). A hopping

regime was used in each case. Further consideration is given to the SICM and BM-SICM responses in the context of charged interfaces in section 5.

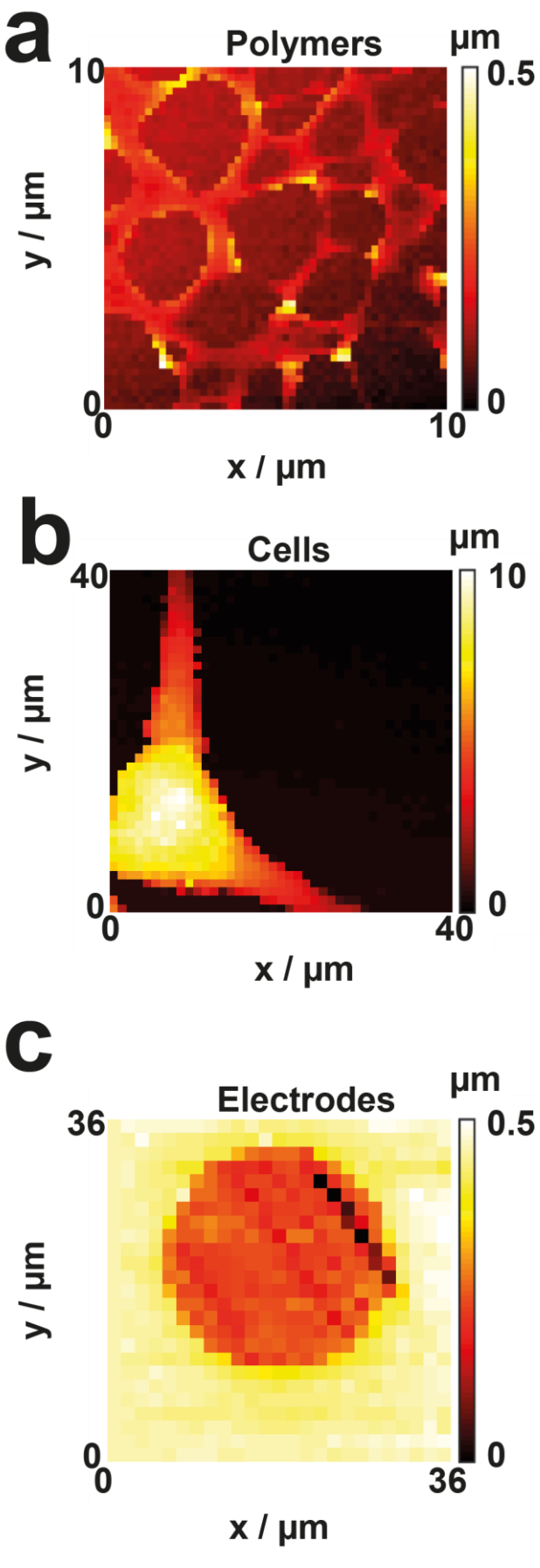
a
Polymers
µm
10
0.5
y / µm
0
0
0
10
x / µm
b
Cells
µm
40
10
y / µm
0
0
0
40
x / µm
c
Electrodes
µm
36
0.5
y / µm
0
0
0
36
x / µm

Figure 4. Topographical imaging with BM-SICM showing: **a)** a polystyrene film on glass; **b)** a PC12 cell and **c)** a gold ultramicroelectrode. Note that there is no interpolation of data, and each pixel shown represents a measurement point.

Whilst modulation techniques hold these notable advantages, opening up more robust imaging capabilities, they can suffer from longer scan times than experiments performed using DC feedback. The extraction of the AC signal using a lock-in amplifier and the inherent response time (which should be approximately 3-4 times the period of oscillation for the acquisition of a reasonable signal) is greater than in the DC mode. In DC-SICM operation, the ionic current responds quickly to changes in the conductance state of the system [59], and with hopping mode the measurement of the tip response in bulk and near-surface at each pixel also provides a robust measurement capability that mitigates against any drift in the response. A comparison of DC and AC modes and the trade-off between speed and precision is considered below (section 5) in the context of surface charge mapping.

2.3 Topographical Imaging of Living Cells

As exemplified by Figure 1d and Figure 4b, the non-invasive (non-contact) nature of SICM, combined with the wide range of possible imaging media, make it particularly suitable for live cell imaging when compared to other SPMs [60]. The first studies of cell morphology using SICM, in 1997 [2,61], highlighted the benefits of the non-contact nature of the technique, showing that there was no damage to cells from the scanning process.

SICM has subsequently been used to investigate the properties of a variety of cell types. Some studies have considered the fluctuation of the cell volume as a

function of time via the acquisition of multiple topographical maps [48,61,62], while others improved the scan rate (image time) to study the dynamics of subcellular structures [50] such as microvilli [63] or processes including exocytosis [64] and the cell cycle [3]. Phenotypic changes in cell morphology [65,66] have also been used as a diagnostic tool for a variety of conditions including heart disorders [67] and Alzheimer's disease [68]. As these applications have been extensively reviewed [4] and since they relate to SICM in conventional operation, we do not consider this type of study further.

2.4 Conductance Measurements, Local Delivery and Sizing

While SICM has been used predominantly for the topographical mapping of living cells, other potential applications were evident in early studies. In the very first SICM study [1], for example, areas of high conductance were used to identify pores in a membrane. Further work has considered the imaging of both synthetic [69,70] and biological [71,72] nanopores, with quantitative measurements of individual nanopores possible [73].

The SICM nanopipette can also be used as a reservoir of analyte (for example DNA) that can then be delivered to a surface in a highly localised manner by controlling the bias of the QRCE in the nanopipette [16,74–78]. Such studies have potential application in the delivery of particular molecules and therapeutics to a specific cell or subcellular region. Recent work has highlighted the extraordinary precision with which nanopipettes can be used to detect and size individual nanoparticles (NPs), by analysis of the resistive pulse caused by the NP being passed, to and fro, through a nanopipette orifice [79], as well as to deliver NPs to an electrode surface [80]. Interesting applications of this type of technology can be envisaged,

where an extremely well characterised NP is delivered to an interface (from cells to materials) and the response used to characterise the interaction of the material with the interface. In this respect, dual channel (theta) micropipettes have already been used to deliver microparticles [81] and polymers [82] to living plant root cells, and this novel microfluidic device could be shrunk down to the nanoscale.

As well as being able to deliver material to a surface, the SICM nanopipette also allows single-cell nano-biopsies to be performed, through the extraction of a small amount of material from inside a cell which is then further analysed [83,84]. This material can be, for example, mRNA, the levels of which can be quantified using PCR. Extraction in this manner is valuable as the subsequent analysis can be tied to cell location, or used to compare the properties of a number of cells in a group.

3. SICM PROBE CHARACTERISATION

As evident from the foregoing discussion, SICM usually employs a single barrelled micropipette or nanopipette as the probe (although other geometries and multichannel probes are possible, as discussed later). Probes are fabricated from either a glass or quartz capillary, which is heated in the centre, typically using a laser puller, which applies a pulling force to each end of the capillary during heating [4]. At the position of the laser heating, the capillary is melted and the pulling force distorts the glass, pulling it finer until the two halves of the capillary separate, yielding two similar nanopipettes with a fine taper at the end. The parameters used in the production of nanopipettes can be varied to produce different geometries, tailored to particular applications. Depending on the heat used, pulling force and material chosen, it is possible for pipettes to be fabricated reliably with openings spanning from several tens of nanometres to the micrometre scale.

In contrast to the traditional (ohmic) view of the SICM response outlined above in Section 2.1, it has recently been shown that many factors, particularly the surface charge density of the sample and the tip, can have a significant effect on the ionic current in the vicinity of the surface [40,47,85]. It is thus imperative that the response of SICM probes is fully understood in order to obtain quantitative information, topographical or other, from the data collected. A key aspect of this analysis is to know the tip geometry.

Nanopipette probes are often assumed to be conical (see section 4 for more details) [45,46] and the size of the nanopipette opening has usually been extracted from ionic conductance measurements [86]. While it is possible to consistently pull probes with diameters in a range of several tens of nanometers, nanopipettes produced in different pulls or on different days can vary in geometry, and it has recently been shown that very small changes in probe geometry can result in measureable differences in the conductance behaviour of the nanopipettes [87]. Scanning electron microscopy (SEM) is used to provide information about the nanopipette geometry near the orifice; a typical SEM image of a nanopipette opening is shown in Figure 5a. However, SEM can only provide information about the nanopipette opening size and outer nanopipette dimensions, forcing assumptions to be made about the nanopipette *inner geometry*. As the nanopipette resistance is extremely sensitive to the nanopipette inner angle and the lumen size, for a significant portion of the nanopipette beyond the aperture, it is important to look inside the nanopipettes using, for example, transmission electron microscopy (TEM) which has recently been shown to be a powerful means of visualising nanopipette geometry [87,88]. Figure 5 compares SEM and TEM images of quartz and borosilicate nanopipettes, illustrating how TEM provides a more complete picture of nanopipette geometry that can be implemented in

models to better understand the ionic current response. Comparisons can be made between nanopipettes pulled from quartz (Figure 5b) and borosilicate glass (Figure 5c) capillaries. Evidently the probes fabricated from these different materials have somewhat different geometries. From TEM measurements, the inner angle of quartz nanopipettes can be seen (Figure 5d) to vary by up to 10° across the region of the pipette, suggesting that the typical assumed conical geometry may not be sufficient to accurately model the SICM response. The parameters extracted from a full characterisation can subsequently be used to model SICM experiments in considerable detail, *vide infra*, and elucidate the contribution of various surface and solution phenomena to the current-potential-time response [87].

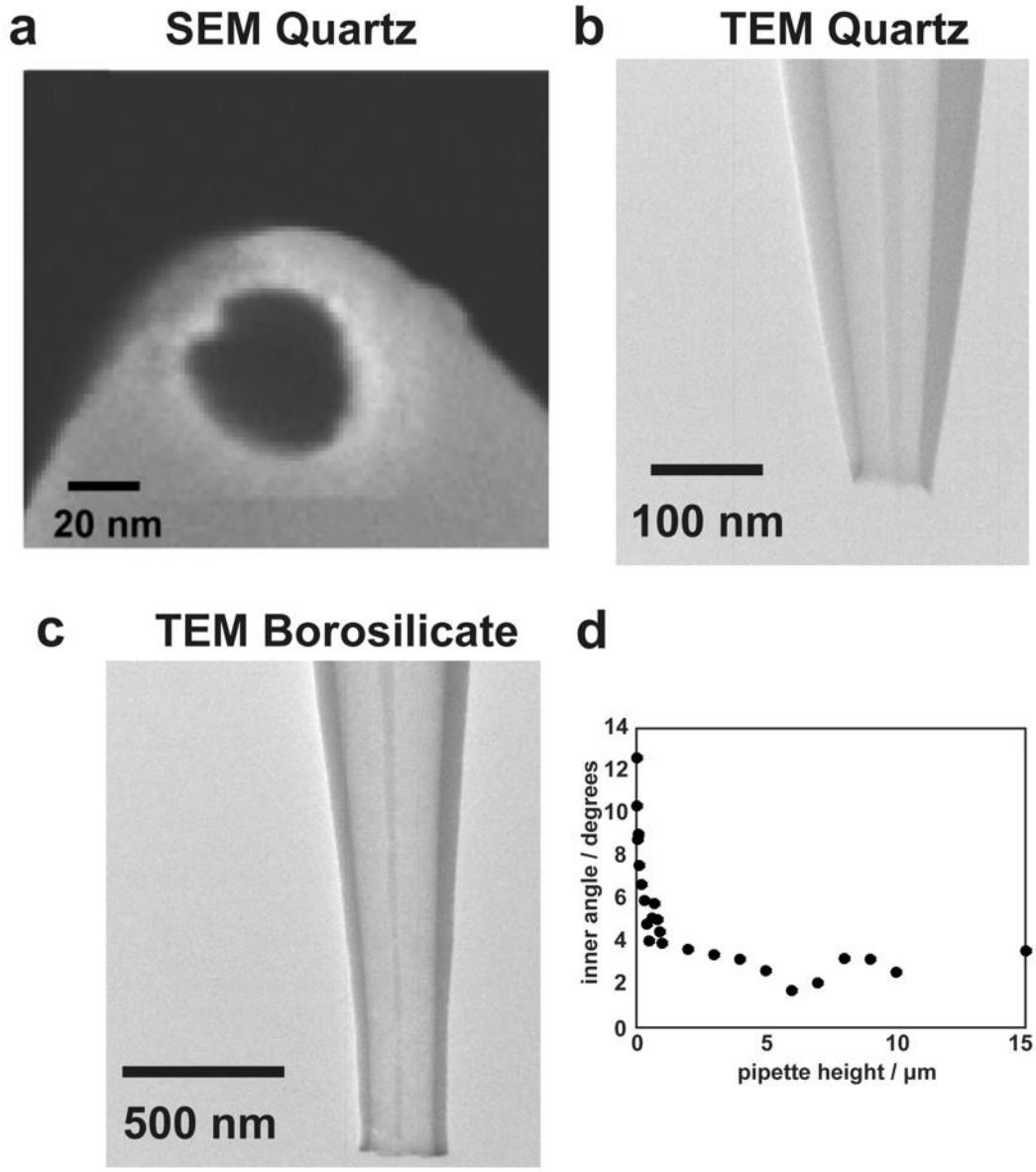

Figure 5. Characterization of nanopipette geometry with SEM and TEM showing typical SEM **(a)** and TEM **(b)** images of quartz nanopipettes and a TEM image of a borosilicate nanopipette **(c)**. **d)** Plot of the inner angle of a typical quartz nanopipette as a function of the height of the nanopipette (measured from the opening). b-d) are reprinted with permission from reference 87. Copyright 2016 American Chemical Society.

4. MODELLING

With multiple inputs (substrate topography, surface charge, local chemical and ion fluxes, applied potential, tip-substrate separation, time etc.) influencing the output (the ionic current), it becomes near impossible to confidently interpret SICM signals without an accompanying theoretical framework. In much of the work discussed in the remainder of this article, a combination of established simple analytical models and computational modelling techniques, specifically finite element method (FEM) simulations, are used to analyse and quantify SICM data. The use of FEM simulations, in particular, is an important aspect of SICM that has recently been developed [42,47,87,89].

Not withstanding the resulting uncertainties (highlighted in the preceding section), when a nanopipette is assumed to have a conical geometry, and the inner cone angle is known or assumed, with surface charge playing no role in the current response [85,90,91], theoretical approach curves (current-distance) to insulating surfaces can readily be produced, for example, by applying equation 1 [4,58]:

$$R_{tip} = R_{bulk} + \frac{\frac{3}{2}\log\frac{r_{out}}{r_{in}}}{K.\pi.d} \quad [1]$$

where r_{out} and r_{in} are the outer and inner radii of the nanopipette at the opening, respectively, d is the separation distance between the end of the tip and the surface and K is the solution conductivity. Such equations are useful approximations, but need to be used with care.

In FEM simulations, computational software, such as COMSOL Multiphysics, as applied in the majority of the studies discussed herein, can be used to solve a specified set of partial differential equations in a defined geometry [87], subject to initial conditions and boundary conditions chosen by the user. A typical FEM model

first involves defining the desired geometry to closely match the experimental system and specifying the necessary material properties of the solution and nanopipette, such as solution viscosity, dielectric constants (of both the pipette and electrolyte) and density. The simulated geometry can be in 1D, 2D, or 3D, with the higher dimensions requiring more computational power, but usually enabling more faithful representation of the experimental setup. Additionally, concentrations, charge number and ion mobility are required for each ionic species present in solution. Other experimental conditions such as chemical reactions and equilibria, as well as temperature, also need to be specified. The equations to be solved are the Nernst-Plank equation, describing the flux of ions and molecules in solution:

$$J_i = -D_i \nabla c_i - z_i \frac{D_i}{\mathrm{R}T} \mathrm{F} c_i \nabla \phi + c_i u \qquad [2]$$

where J_i is the total flux of species i, D_i is the diffusion coefficient of species i, c_i is the concentration of species i, z_i is the charge on species i, R is the universal gas constant, T is the temperature, F is the Faraday constant, ϕ is the electric potential and u is the fluid velocity, and the Poisson equation to describe the electric potential:

$$\nabla^2 \phi = \frac{-\mathrm{F}}{\varepsilon \varepsilon_0} \sum_i z_i c_i \qquad [3]$$

where ε is the relative permittivity of the solvent, typically water [58] and ε_0 is the vacuum permittivity. FEM modelling of steady-state problems involves setting initial conditions as a first approximation and then estimating subsequent solutions until the calculated error has been minimised. Alternatively, time-dependent simulations can be performed, based on the initial state of the system, which help to provide physical

insights into dynamic (transport) processes and timescales [44,92]. We consider here the use of FEM models for the types of SICM studies carried out hitherto, but note that extension to other processes such as mixing [93], crystal growth and dissolution [94], heat transfer problems [95] and the study of electrodes and electrical components [96] is straight forward.

We outline below (section 5) how FEM simulations can be used to understand and predict the current-potential response of a charged nanopipette in the vicinity of a charged interface in an SICM experiment [41,42,44], from which, in turn, surface charge values can be quantified. Additionally, simulations performed in bulk solution can also aid in the characterisation of nanopipette surface properties and response [87]. Utilising TEM to extract the true geometric parameters of a nanopipette, as discussed in Section 3, leaves the surface charge of the nanopipette walls as the only unknown parameter, which can be varied until a match is achieved with experimental measurements, using an appropriate model for the EDL.

In other studies, FEM simulations have helped provide insights into the limitations of SICM including the resolution achievable [86,97]. 3D simulations performed of a nanopipette over a cylindrical pore showed that it was possible to clearly resolve features when they were separated by $3r_{in}/2$, where r_{in} is the radius of the nanopipette opening [97]. Whilst there are some limitations of these simulations, in that they assumed nanopipettes to exhibit a conical geometry, the results help to understand the SICM response and various factors such as the nanopipette size required to achieve a desired resolution, and the tip-surface separation distances that would be needed. It should be noted that there is some discrepancy between simulated and experimental studies of resolution in SICM [98], because experiments have suggested that a resolution as small as $0.5r_{in}$ [98,99] is possible.

FEM simulations can also aid understanding of how the nanopipette response changes with the slope of the sample being probed [100]. This study showed that the change in resistance with distance on approach to a flat sample could be different to that where there is a significant slope of the sample (e.g. cell surface) on the scale of the nanopipette opening. FEM simulations have been useful in implementing algorithms to deal with this and to provide image processing protocols to help correct images of non-planar objects. This involves combining the initial topographical information extracted from SICM experiments with FEM simulations of the nanopipette response and using an iterative procedure to improve the final SICM topographical image [100].

5. FUNCTIONAL SICM: BEYOND TOPOGRAPHY

We consider two main ways in which SICM can be extended beyond topographical imaging to the consideration of function: (i) the design and use of specific voltage (electrochemical) routines combined with the comprehensive modelling of the system to extract functional information in a single barrel setup; and (ii) combining SICM with other techniques, either by the use of multichannel probes or using a second technique in tandem. Sections 5.1 and 5.2 will focus on the first of these two approaches and will comprise the majority of the discussion. An overview of the various techniques used for the second approach is provided in sections 5.3-5.6.

5.1 Surface Charge Mapping

One of the most significant recent advances in SICM has been the development of capability for the mapping of surface charge heterogeneities on extended substrates by sensing variations in the surrounding EDL [40,47], and the development of this

concept to turn SICM into a robust and quantitative tool for unambiguous mapping of both surface topography and surface charge for a range of systems, both biomimetic/materials and living cells [41,42,44,101]. Surface charge is of vital importance in a diverse range of complex interfacial systems, though perhaps most significantly in living systems, where it is known to play a key role in many processes, including cellular growth and division [102,103], adherence [104–106], cellular uptake [107–111], and communication [112–114]. Thus, a robust method of quantitatively resolving spatial heterogeneities in surface charge density adds significant functional power to SICM. In this section of the article we discuss the principles of surface charge mapping with SICM and summarise recent developments.

5.1.1 The Electrical Double Layer

While some solids are neutral (uncharged) in an aqueous environment, ions may adsorb onto the surface or surface groups may ionise, resulting in a net charge at the surface, which leads to the formation of an EDL of ions that are attracted to the charged surface to balance the charge. The size (length normal to the surface), structure, and composition of the EDL strongly depends on the magnitude of the surface charge, the ionic composition and concentration of ions in the bulk fluid [115].

Understanding the structure and properties of EDLs is of great importance in a many areas, including colloidal systems and in the electrochemical behaviour of electrodes [116]. For dilute solutions, and moderate potentials, a Gouy-Chapman model is often reasonable [115], in which the electric potential decays exponentially with distance from the charged surface into solution, so that the EDL is represented as

a diffuse double layer (DDL). For a symmetrical electrolyte, the relationship between surface charge and the surface potential has the form [115]:

$$\sigma = (8RT\varepsilon\varepsilon_0 c \times 10^3)^{1/2} \sinh(\frac{z\psi_0 F}{2RT}) \quad [4]$$

At low potentials, this equation yields the Debye parameter [115]:

$$\kappa = \left(\frac{2F^2 I \times 10^3}{RT\varepsilon\varepsilon_0}\right)^{\frac{1}{2}} \quad [5]$$

where *I* is the ionic strength of the electrolyte solution, whose reciprocal determines the characteristic DDL thickness. It is significant to note that as the value of *I* increases, the characteristic thickness of the DDL decreases.

5.1.2 Ion Current Rectification in Nanopipettes and Nanopores

It is useful to first consider the current-voltage behaviour of a nanopipette in bulk solution. The surface chemistry of the glass or quartz probes means that the surface charge presented in solutions depends strongly on the solution properties such as pH for aqueous solution [117]. The pK_a for the dissociation of silanol groups is about 7.5 [117], although the value depends on the type of glass used, and thus at neutral pH glass usually has a negative surface charge [117]. This, combined with the conical geometry and asymmetric mass transport rates within and outside the nanopipette (or nanopore) results in the phenomenon known as ion current rectification (ICR) whereby the current response to linearly applied bias between a QRCE in the nanopipette and one in bulk solution shows rectification [90,91,118–122]. Figure 6a

presents simulated current-voltage profiles with different surface charge applied to the nanopipette walls in 10 mM KCl solution. It can be seen that the level of rectification, defined as the ratio of the current magnitude at a positive potential to the current magnitude at the same potential at the opposite polarity, varies with the magnitude of applied bias and surface charge [87,89]. When the nanopipette has a negative surface charge, there is an enhancement of the current at negative voltages and a diminution at positive voltages, relative to an ohmic response. When the nanopipette is positively charged, these effects are reversed and the shape of the current-voltage response, and thus the rectification ratio, is the inverse of what is observed for a negatively charged nanopipette.

When the lumen size of a nanopipette is comparable to the size of the DDL, the negative charge at the walls of the nanopipette creates a region where positively charged cations can pass but the flow of anions is restricted. When a negative bias is applied to the QRCE in the nanopipette with respect to that outside in the bulk, there is an accumulation of cations because the diffusion/migration of cations to the nanopipette is greater than the movement of cations up the nanopipette due to the geometry [59]. FEM simulations, presented in Figure 6b highlight this effect. This results in an enhanced conductance in the nanopipette and greater ionic current, as seen in Figure 6a. When no net bias is applied, the concentrations inside and outside the nanopipette are comparable (Figure 6c). However, when the polarity of the bias is reversed (Figure 6d) a depletion zone forms at the end of the nanopipette because movement of cations from the nanopipette is greater than they can be replaced from further inside the probe [42,87,91]. Figures 6e-g show the effect of different levels of surface charge on the amount of accumulation/depletion within the nanopipette at

negative, zero and positive net biases. It can be seen that switching the polarity of the surface charge on the walls flips the concentration levels in the nanopipette and that the amount of accumulation/depletion of cations scales with the applied surface charge.

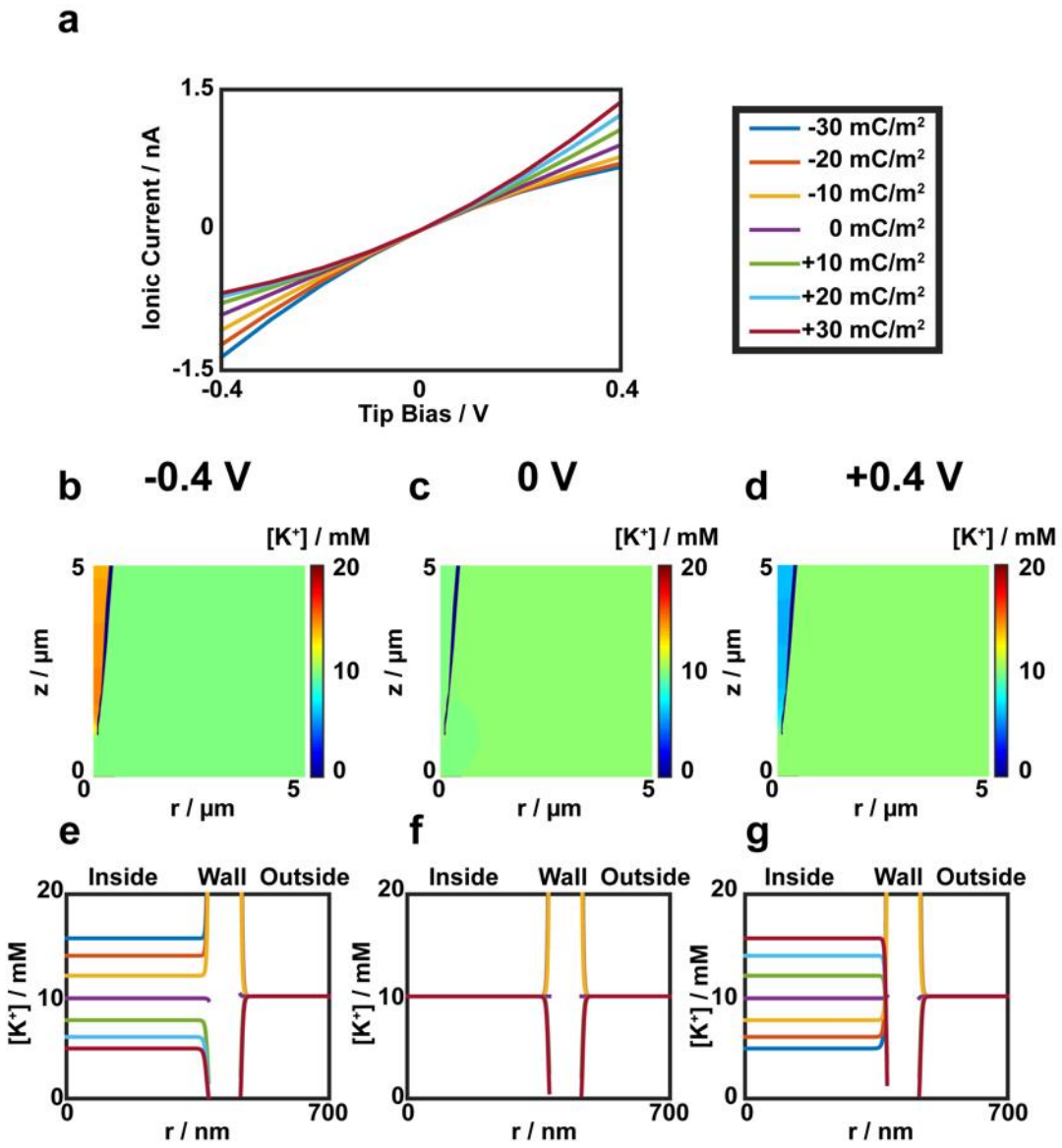

Figure 6. a) Simulated current-voltage curves for a nanopipette in bulk solution with varying surface charge applied to the nanopipette walls. The nanopipette had an opening of radius 90 nm, and the geometry can be gleaned from **(b-d)** which are 2D concentration profiles for a surface charge of -20 mC/m^2 applied to the nanopipette

walls with an initial concentration of 10 mM KCl both in the probe and in bulk and an applied tip bias with respect to the bulk, V_{DC}, of -0.4 V **(b)**, 0 V **(c)** and +0.4 V **(d)**. **e-g)** 1D profiles of K^+ concentration at a fixed height of 4 μm into the pipette, against applied surface charge at -0.4 V **(e)**, 0 V **(f)** and +0.4 V **(g)**. The key for surface charge in **(a)** and **(e-g)** is the same.

The level of ICR observed in nanopipette or nanopore systems depends on the shape and size of the nanopipette: for larger nanopipettes, the effects are much less pronounced and the rectification ratio is closer to unity [120]. ICR is also more prominent when the concentration of the electrolyte in the nanopipette solution is low. At higher electrolyte concentration the surface charge of the walls is screened effectively by ions in solution, compressing the EDL and resulting in a smaller influence of the charge unless the size of the nanopipette is also decreased [91].

The role of electroosmotic flow (EOF) on the ionic current has also been discussed in previous work and has shown to have a minimal effect when the magnitude of the surface charge is small (few mC/m^2) [120]. However, there has not been much study as to the relative contribution when higher surface charge densities are considered. This is an aspect that we discuss further below. Additionally, the relative contribution of surface charge and flow phenomena may be greatly affected by the nanopipette geometry, which is often modelled as being conical, but in practice this is rarely the case, as shown earlier (Figure 5).

5.1.3 Surface Induced Rectification

Whilst ICR in nanopores and nanopipettes has been studied over the last few decades [90,91,120], the impact of surface charge on SICM measurements has been neglected

until recently. The work discussed herein [40–42,44,87] and studies performed in other groups [47,101] has demonstrated that SICM can be used to provide information about the polarity and magnitude of substrate charge. In fact, SICM is sensitive to substrate surface charge for similar tip-substrate distances to which the standard SICM response is observed, ~one tip radius away from the surface [55,99]. The response of the ionic current upon approach to a charged interface differs significantly from that to an uncharged surface, with the response depending on the magnitude and sign of the applied bias, the nanopipette characteristics and ionic strength of the bulk solution [40,41,47]. An understanding of this surface induced rectification (SIR, Figure 7) combined with a suitable scanning regime permits the mapping of surface charge features. Further, surface charge can then be quantified by modelling the SICM setup as described above (section 4).

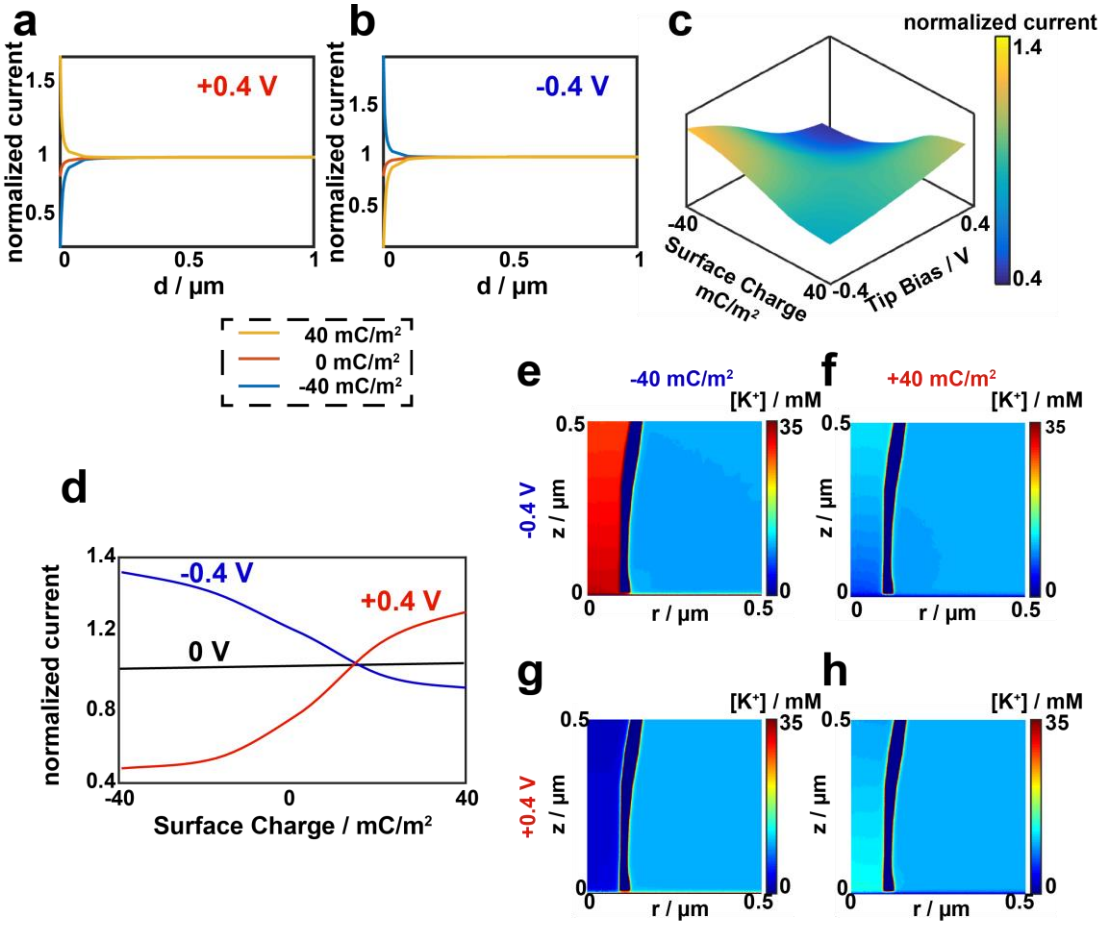

Figure 7. FEM simulated SICM approach curves at **a)** +0.4 V tip bias and **b)** -0.4 V tip bias to different charged surfaces (see key), with tip geometry as defined in **(e-h)**. **c)** Working surface, at a tip-substrate separation of 10 nm, of tip current normalised to the current with the tip in bulk, as a function of substrate charge and tip bias for a nanopipette wall charge of -20 mC/m^2. **d)** Working curves of normalised tip current against surface charge for three tip biases. **e-h)** Concentration profiles in the region of a nanopipette near a positively charged substrate, +40 mC/m^2 **(f,h)** and negatively charged substrate, -40 mC/m^2 **(e,g)** with tip biases of -0.4 V **(e,f)** and +0.4 V **(g,h)**.

Figure 7 illustrates the effects of surface induced rectification phenomena using FEM simulations for a 10 mM KCl solution. As was highlighted in Figure 1, the conventional (established) model for SICM has been that the ionic current should decrease as the nanopipette probe moves within one tip radius of a surface due to the increased resistance caused by the hindrance of ion flow. However, when the QRCE in the nanopipette is held at a negative potential relative to the bulk QRCE and the probe is approached to a negative surface, such as glass, then the ionic current may actually increase. This is observed in Figure 7b for the blue curve, a simulated approach curve to a negatively charged surface (-40 mC/m^2) in which the QRCE in the probe is held at -0.4 V vs. the bulk QRCE. Current enhancements are also observed in these conditions for a positively-biased probe QRCE approaching a positive surface (+40 mC/m^2) [40,47]. In contrast, for a positively charged tip approaching a negatively charged surface (blue curve, Figure 7a), the ionic current is seen to strongly decrease, even more than in the case of an uncharged substrate (orange curve Figure 7a). These results have significant implications for topographical mapping with SICM, the most common application of the technique, as

the approach bias and substrate charge evidently influence the ionic current response. Alternative explanations for current enhancements have been proposed, specifically that the phenomenon results from electroosmotic effects at high ionic strength [123], but this has not been widely accepted. Moreover, as shown below, EOF cannot explain ICR observations.

Figure 7c illustrates further the effects of SIR, presenting a working surface of how the current (normalised to the current measured with the probe in bulk solution) varies with both surface charge and tip bias at a tip-substrate separation of 10 nm (tip radius 90 nm). As described above, when the probe QRCE bias and the surface charge are of the same polarity, current enhancements are observed, whereas at opposite polarities a diminution in the current is seen. It is also worth mentioning that, as the nanopipette walls were negatively charged in these simulations (-20 mC/m^2, as appropriate for glass [47,87]) a stronger enhancement and depletion is observed at negative and positive tip biases, respectively, than if the tip was neutral. From this working surface, individual profiles at different biases can be extracted and show that with increasing bias magnitude, the sensitivity to surface charge increases. Around 0 V, the effect of surface charge on the ionic current is negligible and a near constant decrease of current with distance from bulk irrespective of the substrate surface charge is observed, as would be expected in the traditional SICM response [1,4].

Figure 7e-h presents concentration profiles within the region of the nanopipette near both positively (+20 mC/m^2) and negatively (-20 mC/m^2) charged surfaces with an applied tip bias of either +0.4 V or -0.4 V. The charge on the nanopipette walls was the same as in Figure 6b-d (-20 mC/m^2) and so the data are comparable. It can be seen that with negative tip bias, near a negatively charged substrate, there is an accumulation of cations within the nanopipette and at positive

bias, there is a strong depletion of cations. Similar effects are observed with the nanopipette near a positively charged surface, although the effects are partly diminished by the charge of the pipette walls [47].

As noted above, some previous work suggested that current enhancements on approach to charged interfaces could arise from the effects of EOF [123]. In this work, experimental data was presented in 150 mM NaCl solution that suggested bias dependent current enhancements of over 40% were possible on approaching a glass nanopipette to glass or polystyrene. It is important to note that such significant current enhancements have not been observed in other studies under these conditions [2,4,44] and would unlikely result from a surface charge phenomenon because of the compression of the DDL at these concentrations. Additionally, this work did not include any validation via a simulated response to show that the proposed mechanism of current enhancements was reasonable. Previous studies of nanopipettes both near a surface and in bulk have tried to assess the effects of electroosmosis on the expected ionic current and it has been demonstrated that with low surface charge densities (-1 mC/m^2) on the nanopipette walls in moderate ionic strength (10 mM) the effects of including EOF into simulations results in a small (negligible) impact (<1 %) [40,120].

In order to assess the effect of EOF on SICM experiments under physiological conditions, we have performed FEM simulations with a nanopipette (radius 90 nm, characterised by TEM) positioned both in bulk solution and in the vicinity of a charged interface both in 10 mM and 150 mM KCl solutions, both incorporating EOF, and not including it. As found in previous work, it was seen that EOF had a negligible effect on the expected ionic current when surface charge densities of <5 mC/m^2 were applied to the pipette walls (Figure 8a,b). For higher surface charge densities (-10 mC/m^2) there was a more noticeable change (~8% at the -0.4 V tip bias) to the bulk

ionic current value, as shown in Figure 8c,d. However, it is interesting to note that incorporating EOF into the simulation appears to influence the ionic current in a rather different manner to ICR, in that EOF increases the predicted current at both polarities of tip bias. In spite of this effect of EOF on the ionic current, performing SICM measurements in a self-referencing regime (where the near-surface response is normalised by the bulk response) negates the impact of EOF. For example, for a variety of surface charge densities (-1 mC/m^2, -5 mC/m^2 and -10 mC/m^2) applied to the substrate beneath a nanopipette with surface charge (-10 mC/m^2) applied to its walls, differences of less than 0.5% were predicted, at the extreme potentials explored (± 0.4 V), between normalized current values where EOF had been included and excluded from simulations. It is worth noting that simulations in 150 mM electrolyte solution, similar to that used experimentally [123], do not predict current enhancements at any tip bias, let alone of the magnitude seen and so these SIR observations cannot be explained by EOF.

To summarize, EOF is often excluded from theoretical considerations of nanopipettes both in bulk and near an interface either because it is believed to have a negligible effect [89,91] or because it is computationally expensive to include it. However, as shown herein, it can have some effect on the ionic current in nanopipette experiments when high surface charge densities are on the nanopipette walls. For modelling purposes, it is thus important to first establish whether EOF will have a significant impact and whether excluding it is justifiable. For surface charge measurements, such as those that we have advocated [41,42,44], the self-referencing approach employed - in which near-surface current values are normalised by those with the tip in bulk solution – removes any impact of EOF (within typical

experimental precision), allowing a computationally much cheaper and straightforward simulation.

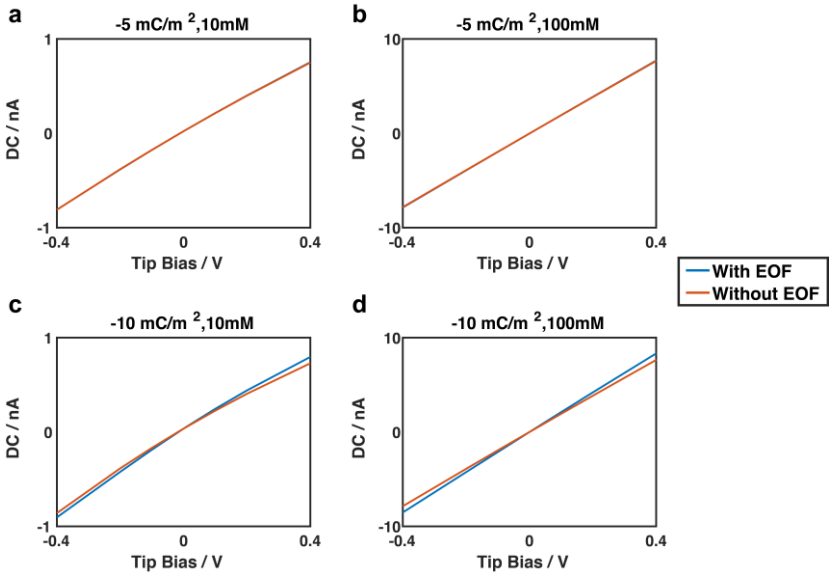

Figure 8. FEM simulated I-V curves with a 90 nm radius nanopipette in bulk solution in **a**) 10 mM KCl, surface charge -5 mC/m^2, **b**) 100 mM KCl, surface charge -5 mC/m^2, **c**) 10 mM KCl, surface charge -10 mC/m^2, **d**) 100 mM KCl, surface charge -10 mC/m^2. Blue lines are simulated results with EOF included, whereas orange lines are the results where EOF is excluded.

As well as using FEM simulations to investigate the effects of SIR, impedance measurements also provide valuable information. Figure 9 presents impedance data collected in 10 mM KCl with a 10 mV oscillation applied on top of specified fixed biases to the nanopipette QRCE in an SICM setup. Similar experiments have been performed in the study of ICR phenomena at nanopipettes in bulk solution, which demonstrated that the charge on the nanopipette walls results in the appearance of multi-time constant impedance loops, depending on the tip bias [124]. Figure 9 presents some initial data, which suggest that similar - but amplified - effects are

observed when a nanopipette is near charged interfaces. At 0 V (Figure 9a), similar behaviour to that observed in high electrolyte is observed (Figure 3c), with the impedance magnitude increasing as the access resistance to the nanopipette increases, at closer tip-substrate separations (labelled ‘Surface’). For conditions where current enhancements are observed (negative tip bias, negative surface), a decrease in the impedance is observed with the nanopipette near the surface, compared to bulk, and a second loop appears in the low frequency regime (Figure 9b). In contrast, at positive tip biases, a second loop appears with the nanopipette near the surface, with increasing impedance at lower frequencies, and the impedance is much larger than with the tip in bulk solution (Figure 9c). These effects were also seen at the opposite tip polarity on approach to a positively charged (3-aminopropyl)triethoxysilane surface. Impedance and BM-SICM measurements complement traditional ionic current measurements and can provide important information for understanding the effects of the EDL on the ion conductance response.

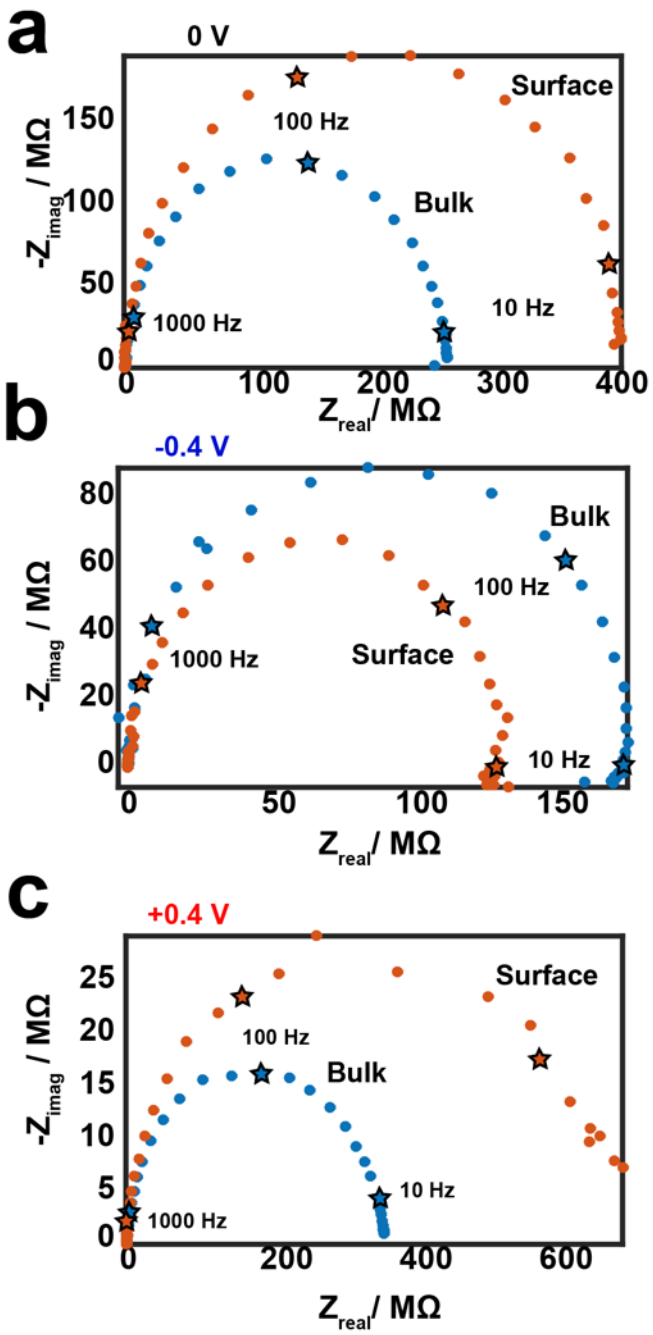

Figure 9. Nyquist plots representing impedance data for an SICM configuration, with a nanopipette in 10 mM KCl aqueous solution (pH ca. 6.5) with a 10 mV oscillation applied on top of a fixed bias of **a)** 0 V, **b)** -0.4 V, **c)** 0.4 V. The nanopipette was positioned either in bulk solution (blue) or near a glass substrate (orange). Data points corresponding to decades in frequency are denoted by stars and labelled according to the frequency.

5.1.4 Application of SICM Charge Mapping to Living Cells

While SIR was initially explored in relatively low electrolyte concentration, it is manifest in solutions up to 150 mM, although not as strongly [42]. Nonetheless, it is an important consideration as this is the ionic strength used in many physiologically relevant experiments. Furthermore, SIR effects are detectable at this ionic strength with relatively large tip sizes (diameters up to 200 nm [42,44]) and the effect would be more significant with smaller tips. As described above, the extent of surface charge influence on the SICM response during the approach of a nanopipette to a surface is dependent on the bias applied between the two QRCEs [41]. At a higher bias, the effect of surface charge is more pronounced, while at a lower bias the convolution is negligible, making 0 V the ideal bias at which to approach a surface and determine topography [41]. This brings BM-SICM [58] to the fore, as zero net bias can be applied.

The effect of SIR on the SICM tip current response, which can then be converted to surface charge density, can be elucidated in the following hopping regime: (i) the topography of the sample, essentially free from surface charge effects, is extracted at zero net bias, using the change in the AC phase between the bulk and surface as feedback (set point) during the approach of the probe; (ii) at each pixel in the topographical image, at the point of closest approach, surface charge is then elucidated by sweeping the bias between the two QRCEs; (iii) this voltammetric response is then compared with a current−voltage curve recorded in bulk solution to reveal any effects of the substrate surface charge. It should be noted that in this regime it is possible to concurrently map both topography and surface charge *essentially independently*, extending the power of SICM far beyond its conventional application as a topographical tool.

The regime described above has been used to probe both model surfaces [41] and living cells [42,44]. Figure 10a shows an optical image of a Baker's yeast cell imaged in 10 mM KCl using BM-SICM (scan area indicated by the black square). The topographical map, extracted with no net bias, is shown in Figure 10b. The normalised current at a probe QRCE bias of -0.4 V with respect to bulk (Figure 10c) shows a sharp contrast between the yeast and the glass support substrate. There is a strong current enhancement near the surface of the yeast cells, relative to the bulk solution, suggesting the presence of a strong negative charge (see simulations in Figure 7d). Figure 10d-f shows data relating to a small scan area on the top of a root hair cell. The BM-SICM technique reveals nanoscale heterogeneities in surface charge. The simultaneously collected topography (Figure 10e) and normalised current (Figure 10f) maps demonstrate the ability of the technique to collect multifunctional information in a single scan with a single-channel probe, simply by making fuller use of the potential-control capabilities in SICM.

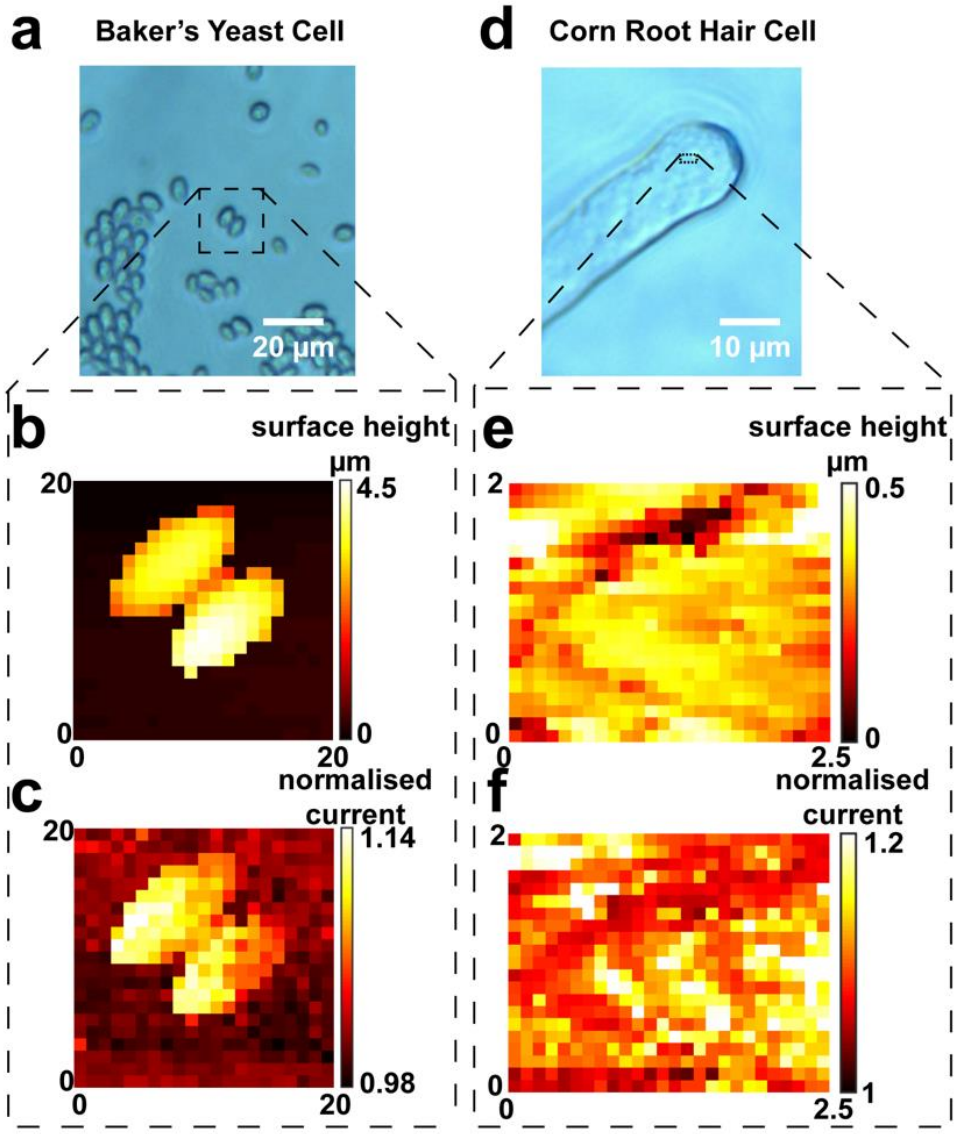

Figure 10. BM-SICM topography and surface charge mapping of Baker's yeast **(a-c)** and root hair cells **(d-f)** in 10 mM KCl with optical image **(a,d)**, topographical data **(b,e)** and normalised ionic current data at a bias of 0.4 V **(c,f)** presented. The scan areas are represented on the optical images by a black dashed square.

As mentioned above, SIR is also seen at higher ionic strength (physiological conditions), for example, in studies of adipocyte cells [42]. Physiological conditions were also employed to demonstrate a second approach for charge mapping, making

use of a pulsed potential chronoamperometric regime [44]. This increases the pixel acquisition rate by over an order of magnitude, with scope for further gains. A DC mode is used for enhanced speed, but to minimise the convolution of surface charge, the approach bias is minimised to a few mV (precise value depending on tip size and electrolyte concentration). Once the surface is detected (topography), the probe is fixed in position and the potential is pulsed to a value where the SICM current is more sensitive to surface charge (higher magnitude bias). This pulse need only be of a few ms duration. Figure 11a presents a topographical map of a PC12, neuron-like, cell obtained using this approach. Current-time curves were collected in bulk and near the substrate at each pixel to elucidate surface charge effects precisely (Figure 11b). By taking the normalised current value (tip current at surface divided by bulk response at a particular time, Figure 11c) and utilising time-dependent FEM simulations of the experimental geometry to generate a current-surface charge working curve (Figure 11d), it becomes possible to quantify the surface charge present on the surface (Figure 11e).

It is important to note that the accuracy of surface charge estimation is predicated on the model used for the EDL. We have chosen a Gouy-Chapman model for the EDL at both the nanopipette and the substrate surface, as also used in many studies of rectification in glass and quartz nanopipettes [59,91,120] with electrolyte concentrations up to 100 mM [120]. As mentioned above, the Gouy-Chapman model is strictly applicable to low ionic strengths and small surface potential. However, for insulating materials, including the glass/quartz nanopipette and cell membranes, the surface charge often arises from a fixed number of sites which restricts ion concentrations in the EDL near the surface even at moderate to high ionic strengths [125,126]. As a consequence, the model has been used at supporting electrolyte

concentrations of the order of 100 mM [127,128]. An advantage of using the DDL for the EDL, as opposed to alternatives for solid surfaces [129] and cell membranes [130] is that only a few, well posed, parameters are needed, avoiding additional arbitrary assignment of parameters (including ion binding parameters) as needed for alternative models, such as a Stern-Gouy-Chapman model [130]. Furthermore, surface force apparatus has been used to demonstrate that the potential profile fits the Gouy-Chapman model at separations of greater than 2 nm from the surface in 1:1 electrolyte concentrations of up to 100 mM [128]. As SICM is being used to probe the DDL from a distance of tens of nanometres [42,44], Gouy-Chapman is the most suitable model for the EDL. In general, it is recognised that more sophisticated descriptions of the EDL are needed and SICM measurements could have a significant role to play in assessing models from simulations of the EDL [131], although very small SICM probes would be needed that could be stationed very close to the substrate surface being probed.

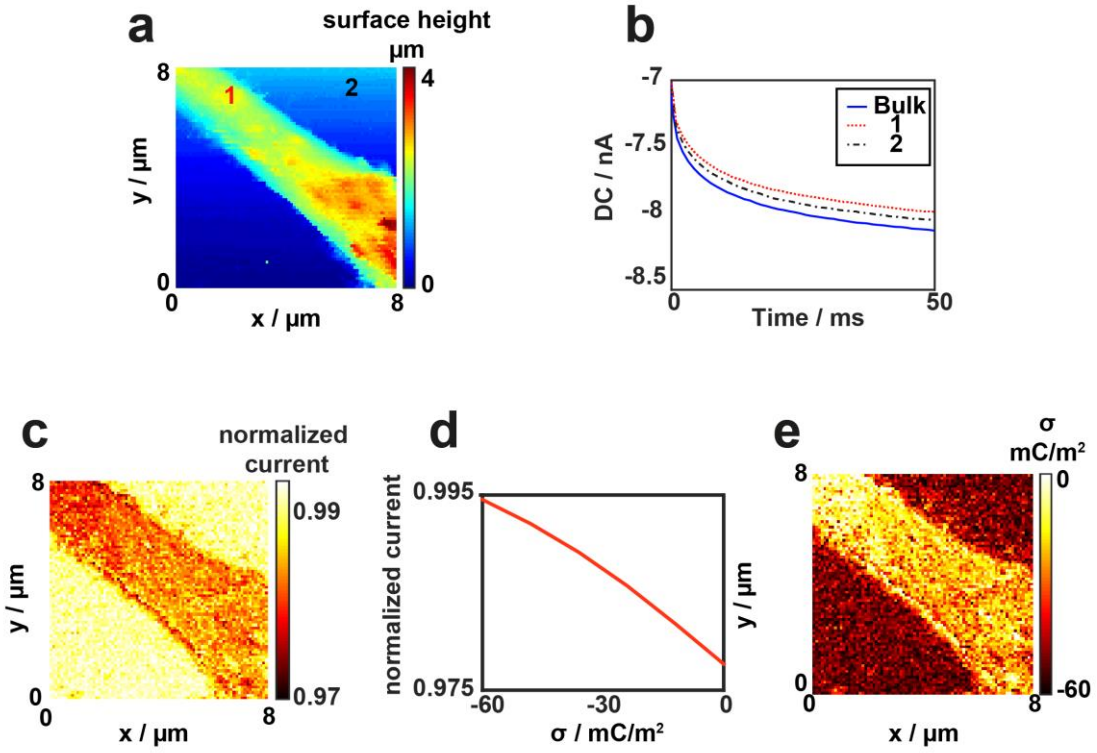

Figure 11. Surface charge mapping of a PC12 cell in physiological conditions, RPMI cell media (~150 mM ionic strength), using pulse potential SICM. **a**) Topographical map obtained at an approach bias of +20 mV. **b**) Example current-time curves extracted in bulk and near the substrate (over the cell and glass support, see part (**a**) for locations) after pulsing the applied bias at the probe QRCE to -400 mV vs. bulk. **c**) Map of normalised SICM current (current from the surface pulse divided by current during bulk pulse at 50 ms). **d)** Simulated working curve at 50 ms to convert **(c)** to surface charge values (**e**) at the probe working distance of 30 nm. This figure is adapted with permission from reference 44 Copyright 2016 American Chemical Society.

5.2 Flux Imaging

A second example of how a full theoretical interpretation of the ionic current response has permitted the application of SICM to functional mapping is the resolution of nanoscale fluxes arising from interfacial reactions [43]. Any reaction that produces or consumes charged species will change the local conductivity (ion composition) of the solution and this can be detected via the local ionic current signal at the SICM probe with appropriate potential control. Tuning the potential of the probe QRCE with respect to the bulk QRCE can either make the response sensitive (negative probe potential in the example in Figure 12a) or insensitive (positive probe potential for the example in Figure 12b) to the changing ionic environment at the surface. This selective (and tuneable) potential-dependent sensing of either the topography or local activity was verified by FEM modelling (Figure 12c,d). It was also possible to separate topography and activity by applying a potential such that the SICM current response was sensitive to local changes in conductivity (reactivity) and oscillating the

nanopipette in a DM mode. The AC amplitude was shown to be relatively insensitive to local reactivity and could be used for topographic feedback, whilst the DC ionic current resolved differences in local reactivity. This approach was applied to the case of hydrazine oxidation and proton reduction (Figure 12e) in a hopping mode with a substrate CV measurement at each pixel (tip potential fixed). Proton reduction leads to a decrease in the local conductivity whilst hydrazine oxidation produces protons and increases the conductivity, giving a higher normalised current (Figure 12f). High-speed electrochemical reaction mapping of flat samples with SICM has also been demonstrated, where electrochemical reactivity maps with 16,250 pixels were generated every 4 seconds [43].

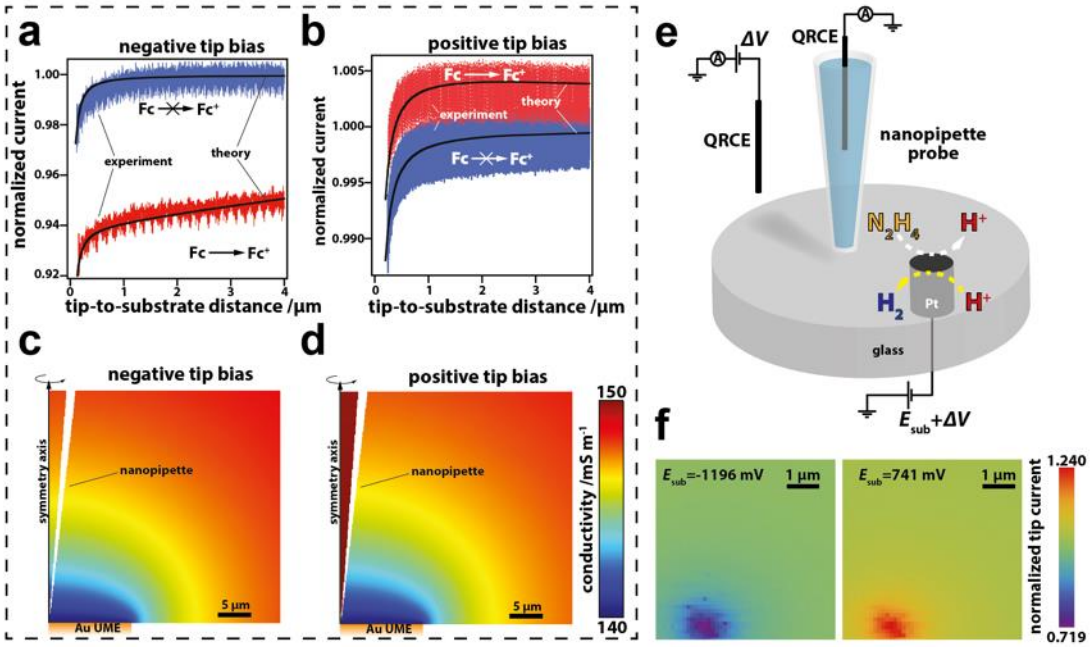

Figure 12. a,b) Experimental (red and blue traces) and simulated (solid black lines) SICM current-distance curves acquired with a nanopipette (biased at −0.1 and +0.1 V, respectively) positioned over an inert (blue) and Fc^+ generating (diffusion-controlled rate) from the oxidation of Fc (Ferrocene methanol) in bulk solution (1.95 mM) at a 12.5 µm radius Au UME (red). Note the difference in scales between (**a**) and (**b**). Tuning the tip potential makes the SICM response sensitive (**a**) or relatively immune

(**b**) to the substrate reaction. **c,d)** Simulated conductivity distributions (magnified view) with a nanopipette (biased at ± 0.1 V) positioned at 1 μm distance from an Fc^+ generating substrate electrode (Au UME). **e)** Schematic representation of the experimental setup employed for mapping hydrazine oxidation and proton reduction at ~600 nm radius Pt UME. **f)** Electrochemical images from a 380-snapshot image sequence, constructed from voltammetric data resolved at each image pixel. The nanopipette current has been normalised by the value at the point of the closest approach (at each individual pixel) with the substrate potential held at −0.2 V (no substrate reaction). Adapted with permission from reference 43 Copyright 2016 American Chemical Society.

Given the multiple applications of single-barrelled SICM it is important to consider the possible convolution of responses between, for example, surface charge and flux imaging. In principle, it should be possible to separate the two functional signals, and obtain topographical information, by exploiting the potential-time control functions that we have implemented, and making measurements at a range of (positive and negative) potentials, in combination with a robust model of the setup. For the systems considered hitherto, the issue of functional convolution has not arisen, i.e. either surface charge or reactivity has dominated. For example, when mapping the surface charge of cells, the ion flux from individual ion channels will have a comparatively negligible effect on the SICM current signal, and – if desired - this can easily be checked by making measurements of surface charge at extreme positive and negative potentials, as we have done [41,42,44], where any ion channel flux would be manifested differently in the SICM response.

5.3 Open Dual-Barrel Techniques

Dual-channel nanopipettes provide additional functionality for SICM, with the simplest type of probe being based on a 'theta' pipette, containing two open barrels (Figure 13a). There have been several applications of such probes. An early application was the independent deposition of DNA, one channel containing DNA stained with alexa 647 and the other DNA stained with rhodamine green [132], allowing the printing of two-component, graded images on a polyethyleneimine modified glass surface. This type of approach was recently advanced to create 3D Cu nanostructures [39], with one barrel used for SICM feedback while the other served as a reservoir of Cu^{2+} ions that were then reduced at the Au substrate (Figure 13a). This technique was able to deposit structures with very high aspect ratios and a critical dimension of less than 1 μm, a significant improvement on previous work using FluidFM [133,134], in which a hollow AFM tip and fluid feed-through in the cantilever is used for deposition. Simple pillars (Figure 13b) and more complex structures (Figure 13c) were deposited (written), which could then be scanned again (read) using the SICM channel to generate high resolution topographical images (Figure 13d). This ability to both build features and verify their construction with the same probe in-situ has added significant new functionality to SICM.

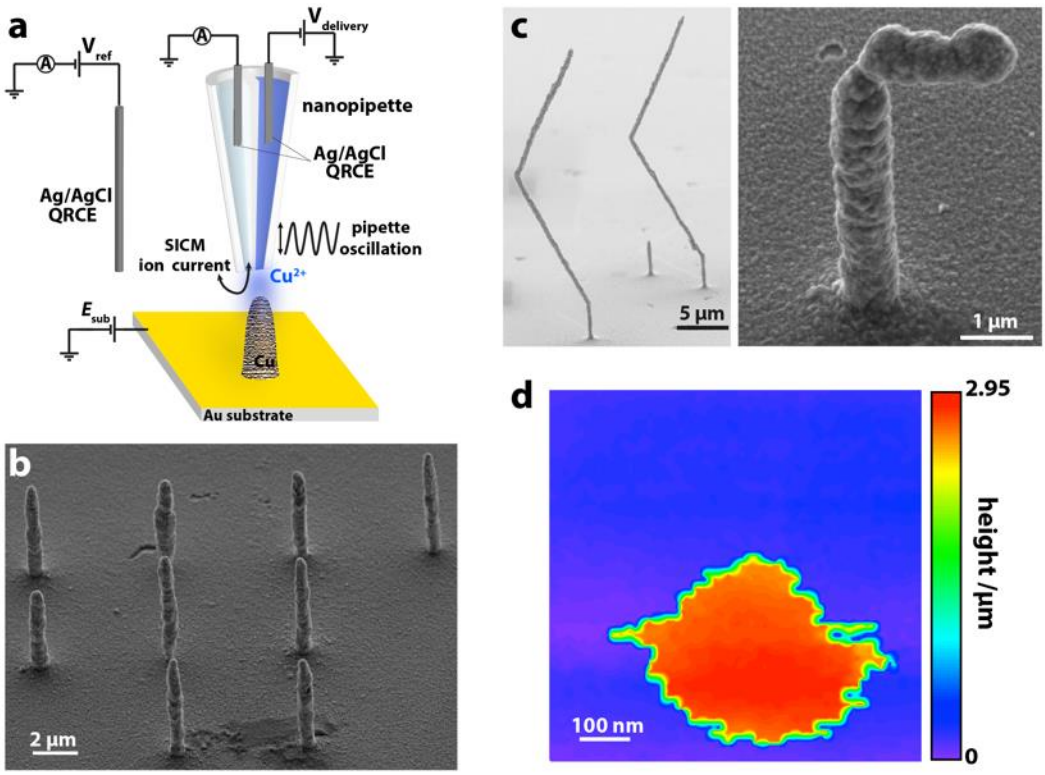

Figure 13. Deposition of Cu nanostructures with a dual-barrel nanopipette. **a)** Schematic of the experimental setup, with one barrel of the theta pipette used for SICM feedback and the other used as a source of Cu^{2+} ions. **b)** Array of nine pillars deposited at a substrate potential of -0.75 V (vs. Ag/AgCl QRCE with an SICM bias of 0.2 V and a bias in the Cu reservoir barrel of 1 V (vs. same QRCE). The deposition time was 60 s and the probe was translated away from the surface under positional feedback control during the growth of each feature. **c)** Example scanning electron micrographs of Cu nanostructures created by retracting vertically before moving laterally with and without feedback to create zig-zag and gamma structures (left and right hand images respectively). **d)** Hopping mode SICM image of a deposited Cu pillar, taken with the same nanopipette probe as used for patterning. Adapted with permission from reference 39. Copyright 2016 American Chemical Society.

The development of potentiometric scanning ion conductance microscopy (P-SICM) [88,135–138] has added further functionality to the theta pipette, permitting the simultaneous measurement of both topography and conductance across membranes. The setup for P-SICM (Figure 14a) requires the application of a bias between electrodes on each side of the membrane to drive trans-membrane ion flow. One barrel of a dual-channel pipette is then used for SICM topographical feedback while the other measures the local conductance near the end of the pipette in a potentiometric regime. This setup has been applied to model nanopores in a polymer membrane (Figure 14b) [135] and to channel conductance at tight junctions (Figure 14c) [88,135,136], with applications including the demonstration that claudin-2 (a protein found in tight junctions) regulates permeability at the junctions of some epithelial cell strains (Figure 14d) [135]. Further work with theta pipettes has included the incorporation membrane patches into one channel of the pipette [139] and using one channel for topographical feedback while the other collects mRNA [84].

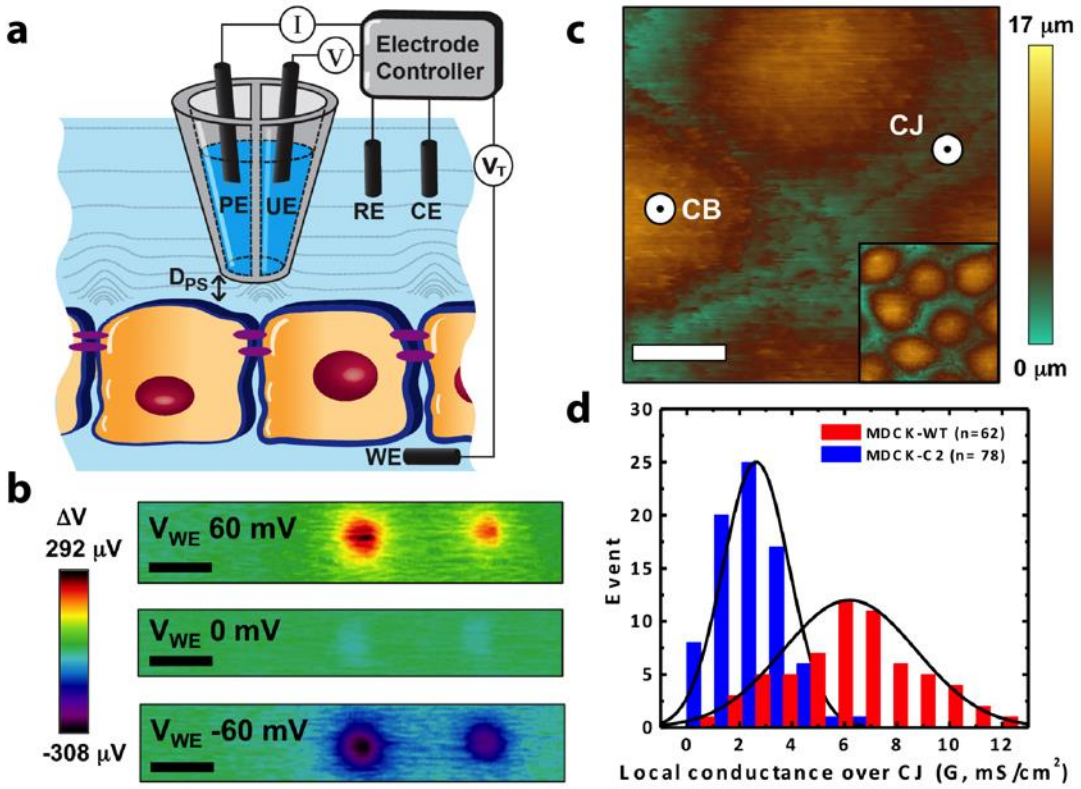

Figure 14. Potentiometric scanning ion conductance microscopy (P-SICM). **a)** Schematic of the P-SICM experimental setup. A bias is applied between the working electrode (WE) and the counter electrode (CE) while the pipette electrode (PE) measures topography and the potential electrode (UE) records the local potential at the pipette tip to make conductance measurements. All electrode potentials are referenced to a single reference electrode (RE). **b)** Local potential variation at nanopores in a polymer membrane at three different transmembrane potentials, measured using P-SICM in imaging mode. Scale bar = 1 μm. **c)** Topographical image of the surface of a cell monolayer shows the position of cell bodies and cell junctions. Scale bar = 5 μm. The inset shows the zoom out image of the cell monolayer under study (40 x 40 μm). CB indicates the cell body and CJ the cell junction. **d)** Histograms of conductances measured at cell junctions for two cell strains (MDCKII-WT and MDCKII-C2, red and blue respectively) using P-SICM, showing that

claudin-2 regulates epithelial permeability. **b-d**) are reproduced with permission from Dr Lane A. Baker from reference 88. Copyright 2014, The Electrochemical Society.

5.4 SECM-SICM

In contrast to SICM, SECM often makes use of the faradaic current signal at a probe (solid or liquid/liquid interface) due to a charge (ion or electron) transfer reaction and can be used to obtain electrochemical maps of a wide variety of interfaces [14,19]. As mentioned in the Introduction (section 1), in comparison to SICM, the topographical capabilities of SECM are often rather poor and the SECM response is much more susceptible to effects of electrode fouling, and from the convolution of topography and activity in the response [21,29]. These limitations can be overcome by combining SECM and SICM into a single probe (SECM-SICM). Two types of SECM-SICM probes have been described: (i) using a dual-barrelled 'theta' pipette where one barrel serves as the SICM channel and the other is a solid SECM electrode [30,32,140,141]; or (ii) by using a ring configuration where metal is deposited on the walls of the SICM channel and is used for SECM imaging [28,29,31]. The theta configuration is used most and is simple to make.

SICM-SECM has recently been used to detect the delivery and uptake of molecules to a cellular surface, with the SECM barrel used to monitor the flux of a molecule of interest, delivered from the SICM barrel, which also tracked the substrate topography [141]. A self-referencing hopping mode was used in which the SECM and SICM channels were calibrated at each pixel. This allowed precise sub-cellular measurements of molecular uptake rates and the protocol was particularly important to avoid complications from substantial drift (deterioration) of the SECM response. SICM-SECM has also been employed for pH sensing [140,142], allowing the

acquisition of simultaneous topography-potentiometric pH maps of surfaces. Functionalization of a carbon electrode in the SECM-SICM setup with platinum has also permitted measurements of O_2 [143,144] and H_2O_2 [145] by amperometry. SICM-SECM has facilitated studies of the electrochemical properties of a wide range of different substrates ranging from dissolving crystals [140] and single living cells [144] to electrocatalytic nanoparticles [30,145] and electrode surfaces [29]. It is expected that these applications will grow in the future.

5.5 Other Hybrid SICM Techniques

Several studies have attempted to further combine SICM with other techniques. For example, SICM-AFM, in which a bent nanopipette serves both as a cantilever and also as an open channel to probe conductance. This type of device has been used for both conductance-topography [146] and topography-force measurements [147,148]. The use of confocal microscopy in tandem with SICM has allowed the simultaneous collection of sample topography and the spatial distribution of fluorescent molecules or particles of interest [149]. This approach has been used to study endocytic pathways [150], such as probing the mechanism of clathrin-coated pit closure [151]. Additionally fluorescence measurements have been very valuable in following the dynamics of delivery from nanopipettes and the behaviour of the fluorescent moieties whilst in a nanopipette [75,152]. These studies showed that it was possible to deliver a single fluorescent molecule to different subcellular regions of a boar spermatozoon and track the diffusion therein [152]. SICM has also been combined with scanning near field optical microscopy to combine optical measurements with ion conductance information [153].

5.6 Further Conductance Techniques

A notable technique that employs ion conductance measurements for positioning [154] or to map ion fluxes [92] is SECCM, a droplet-based electrochemical imaging technique, which does not require the substrate of interest to be bathed in electrolyte solution [154,155]. In this configuration a dual-barrelled pipette is used with both channels filled with electrolyte solution and a QRCE. A meniscus forms at the end of the pipette and, with a bias applied between the two QRCEs, an ion conductance signal is produced. When the droplet contacts with a substrate, the meniscus changes shape and this is detected in the conductance response. By recording the probe position required to maintain a constant conductance value, as the droplet is scanned across a substrate, SECCM can be used to map topography of insulating or conducting samples [96,154]. Additionally, through the inclusion of redox-active species in the SECCM barrels, electron transfer between probe molecules and a working substrate electrode can be studied in a highly localised manner [156]. In this way, heterogeneities in surface activity can be identified through variations in the faradaic current at the working electrode, defined by the mobile meniscus cell. SECCM has been used extensively to obtain major new insights into the behaviour of carbon electrodes including: graphene [96,157], carbon nanotubes [158,159] and boron doped diamond [160] as well as for studying other electrode materials [161] and individual catalytic nanoparticles [162,163]. All of these materials find application in bioelectroanalysis, and the deeper understanding of structure-activity revealed by SECCM, in tandem with complementary microscopy methods applied to the same area in a correlative multimicroscopy approach [12,164], is hugely valuable for the development of next generation sensors and electrocatalysts.

As with SICM, droplet techniques allow for the controlled deposition and delivery of material to a substrate allowing for complex patterning and formation of microstructures on an electrode or other substrate [132,165]. Furthermore, such probes can be used to make local dissolution measurements [92], including of biominerals such as dental enamel, and the assessment of treatments to protect the tooth surface [166]. Additional channels can be added to the probe to make multiple ionic current and electrochemical measurements [167]. An in depth consideration of the SECCM technique can be found in a recent review [155].

6. CONCLUSIONS

Although SICM was invented more than a quarter of a century ago, it is only in recent years that its full potential as a multi-functional tool has been realised. SICM has long been recognised as a powerful instrument for mapping topography of a wide range of different substrates, most prominently living cells, where the non-contact nature of the technique is particularly beneficial for measurements at soft samples. Further, SICM is a simple but versatile tool for the precise delivery of molecules to a desired location on a substrate and is able to make high-resolution conductance measurements, with applications to membrane transport. These are established capabilities of SICM that make the instrument valuable for various life sciences applications.

The main focus of this article has been to highlight new developments, spanning novel control functionality, a deep understanding of the electrochemical properties and principles underpinning the response, new types of scan regimes and feedback protocols that turn SICM into a very powerful multifunctional technique capable of probing new processes, such as surface charge and ion flux processes through careful monitoring of changes in the nanopipette conductance. Furthermore,

by combining SICM with other microscopy techniques, for example confocal microscopy and SECM, considerable additional functionality is added that provides a promising outlook for future studies using multi-barrelled nanopipette probes. An important aspect in the recent advance of SICM has been the development of a robust theoretical framework for understanding the substrate-solution interface and probe response, an important aspect that we have considered herein. We have assessed the physicochemical phenomena that can contribute to the SICM response and how they can best be accounted for and modelled. This theoretical foundation, together with methods for the exact characterisation of nanopipette probes, means that quantitative information can be extracted from SICM measurements.

SICM is very much suited for the study of living systems and there is a vast range of information that can be obtained through control of the SICM potential-time and scan regimes. Ion conductance measurements are expected to play a key role in the future for elucidating valuable information about cellular function, and correlating the surface properties of cells with physiological function. Some of the proof of concept studies outlined herein serve as a roadmap for what may be possible.

COMPETING INTERESTS

We have no competing interests.

AUTHORS' CONTRIBUTIONS

Much of the experimental work presented herein was carried out by DP and to a lesser extent by AP. All three authors had significant input into planning and writing the manuscript. PRU conceived the article, supervised the majority of the experimental

work discussed herein and led the revision of the manuscript, following an initial draft from AP and DP. All authors gave final approval for publication.

ACKNOWLEDGEMENTS

The authors would like to thank the many members of the Warwick Electrochemistry and Interfaces Group (WEIG), who have contributed to some of the published work discussed herein, and Dr. Alex Colburn for the custom-built electronics equipment used by the members of WEIG. We also thank Dr. Lane Baker for kindly providing the images in Figure 14.

FUNDING

This work was supported by the EPSRC through the MOAC DTC, grant no. EP/F500378/1 (AP) and the Leverhulme Trust through a research project grant (DP and PRU).

LIST OF ABBREVIATIONS

AC	Alternating Current
AFM	Atomic Force Microscopy
BM	Bias Modulation
CV	Cyclic Voltammogram
DC	Direct Current
DDL	Diffuse Double Layer
DLM	Diffuse Layer Model
DM	Distance Modulation
DNA	Deoxyribonucleic Acid

EDL	Electrical Double Layer
EOF	Electroosmotic Flow
FEM	Finite Element Method
ICR	Ion Current Rectification
mRNA	Messenger Ribonucleic Acid
NP	Nanoparticle
P-SICM	Potentiometric-SICM
PCR	Polymerase Chain Reaction
QRCE	Quasi-Reference Counter Electrode
RPMI	Roswell Park Memorial Institute (medium)
SECCM	Scanning Electrochemical Cell Microscopy
SECM	Scanning Electrochemical Microscopy
SEM	Scanning Electron Microscopy
SICM	Scanning Ion Conductance Microscopy
SIR	Surface Induced Rectification
SPM	Scanning Probe Microscopy
STM	Scanning Tunnelling Microscopy
TEM	Transmission Electron Microscopy
UME	Ultramicroelectrode

LIST OF SYMBOLS

C	Capacitance
c_i	Concentration of species i
d	Distance between probe and substrate
D_i	Diffusion coefficient of species i

F	Faraday constant
I	Ionic strength
J_i	Total flux of species i
R	Gas constant
r_{in}	Inner probe radius
r_{out}	Outer probe radius
R_{acc}	Access resistance
R_{bulk}	Bulk solution resistance
R_p	Probe resistance
R_{tip}	Total tip resistance
u	Fluid velocity
z_i	Charge on species i
Z_{real}	Real component of impedance
Z_{imag}	Imaginary component of impedance
ε	Relative permittivity of the solvent
ε_0	Vacuum permittivity
K	Solution conductivity
κ	Debye parameter
σ	Surface charge
ϕ	Electric potential
ψ_0	Surface potential

REFERENCES

1. Hansma, P. K., Drake, B., Marti, O., Gould, S. A. & Prater, C. B. 1989 The scanning ion-conductance microscope. *Science (80-.).* **243**, 641–643. (doi:10.1126/science.2464851)
2. Korchev, Y. E., Bashford, C. L., Milovanovic, M., Vodyanoy, I. & Lab, M. J.

1997 Scanning ion conductance microscopy of living cells. *Biophys. J.* **73**, 653–658. (doi:10.1016/S0006-3495(97)78100-1)
3. Gorelik, J. et al. 2004 The use of scanning ion conductance microscopy to image A6 cells. *Mol. Cell. Endocrinol.* **217**, 101–108. (doi:10.1016/j.mce.2003.10.015)
4. Chen, C.-C., Zhou, Y. & Baker, L. A. 2012 Scanning Ion Conductance Microscopy. *Annu. Rev. Anal. Chem.* **5**, 207–228. (doi:10.1146/annurev-anchem-062011-143203)
5. Meyer, E., Hug, H. J. & Bennewitz, R. 2013 *Scanning probe microscopy: the lab on a tip*. Springer Science & Business Media.
6. Binnig, G. & Quate, C. F. 1986 Atomic Force Microscope. *Phys. Rev. Lett.* **56**, 930–933. (doi:10.1103/PhysRevLett.56.930)
7. Rugar, D. & Hansma, P. 1990 Atomic force microscopy. *Phys. Today* **43**, 23–30. (doi:http://dx.doi.org/10.1063/1.881238)
8. Binnig, G. & Rohrer, H. 1983 Scanning tunneling microscopy. *Surf. Sci.* **126**, 236–244. (doi:10.1016/0039-6028(83)90716-1)
9. Hansma, P. K. & Tersoff, J. 1987 Scanning tunneling microscopy. *J. Appl. Phys.* **61**. (doi:10.1063/1.338189)
10. Bard, A. J., Fan, F.-R. F., Kwak, J. & Lev, O. 1989 Scanning Electrochemical Microscopy. Introduction and Principles. *Anal. Chem.* **61**, 132–138. (doi:10.1021/ac00177a011)
11. Kwak, J. & Bard, A. J. 1989 Scanning electrochemical microscopy. Apparatus and two-dimensional scans of conductive and insulating substrates. *Anal. Chem.* **61**, 1794–9. (doi:10.1021/ja3106434)
12. Kang, M., Momotenko, D., Page, A., Perry, D. & Unwin, P. R. 2016 Frontiers in Nanoscale Electrochemical Imaging: Faster, Multifunctional and Ultrasensitive. *Langmuir* **32**, 7993–8008. (doi:10.1021/acs.langmuir.6b01932)
13. Kranz, C. 2014 Recent advancements in nanoelectrodes and nanopipettes used in combined scanning electrochemical microscopy techniques. *Analyst* **139**, 336–52. (doi:10.1039/c3an01651j)
14. Polcari, D., Dauphin-Ducharme, P. & Mauzeroll, J. 2016 Scanning Electrochemical Microscopy: A Comprehensive Review of Experimental Parameters from 1989 to 2015. *Chem. Rev.* **116**, 13234–13278. (doi:10.1021/acs.chemrev.6b00067)
15. Takahashi, Y., Kumatani, A., Shiku, H. & Matsue, T. 2016 Scanning Probe Microscopy for Nanoscale Electrochemical Imaging. *Anal. Chem.* **89**, 342–357. (doi:10.1021/acs.analchem.6b04355)
16. Laslau, C., Williams, D. E. & Travas-Sejdic, J. 2012 The application of nanopipettes to conducting polymer fabrication, imaging and electrochemical characterization. *Prog. Polym. Sci.* **37**, 1177–1191. (doi:10.1016/j.progpolymsci.2012.01.002)
17. Lee, C., Kwak, J. & Bard, A. J. 1990 Application of scanning electrochemical microscopy to biological samples. *Proc. Natl. Acad. Sci. U. S. A.* **87**, 1740–1743. (doi:10.1073/pnas.87.5.1740)
18. Macpherson, J. V. & Unwin, P. R. 1995 Scanning Electrochemical Microscopy as a Probe of Silver Chloride Dissolution Kinetics in Aqueous Solutions. *J. Phys. Chem.* **99**, 14824–14831. (doi:10.1021/j100040a037)
19. Amemiya, S., Bard, A. J., Fan, F.-R. F., Mirkin, M. V. & Unwin, P. R. 2008 Scanning Electrochemical Microscopy. *Annu. Rev. Anal. Chem.* **1**, 95–131. (doi:10.1146/annurev.anchem.1.031207.112938)

20. Schulte, A., Nebel, M. & Schuhmann, W. 2010 Scanning electrochemical microscopy in neuroscience. *Annu. Rev. Anal. Chem. (Palo Alto. Calif).* **3**, 299–318. (doi:10.1146/annurev.anchem.111808.073651)
21. Sun, T., Yu, Y., Zacher, B. J. & Mirkin, M. V. 2014 Scanning electrochemical microscopy of individual catalytic nanoparticles. *Angew. Chemie - Int. Ed.* **53**, 14120–14123. (doi:10.1002/anie.201408408)
22. Izquierdo, J., Nagy, L., Varga, Á., Bitter, I., Nagy, G. & Souto, R. M. 2012 Scanning electrochemical microscopy for the investigation of corrosion processes: Measurement of Zn2+ spatial distribution with ion selective microelectrodes. *Electrochim. Acta* **59**, 398–403. (doi:10.1016/j.electacta.2011.10.076)
23. Shen, M., Ishimatsu, R., Kim, J. & Amemiya, S. 2012 Quantitative imaging of ion transport through single nanopores by high-resolution scanning electrochemical microscopy. *J. Am. Chem. Soc.* **134**, 9856–9859. (doi:10.1021/ja3023785)
24. Varga, Á., Nagy, L., Izquierdo, J., Bitter, I., Souto, R. M. & Nagy, G. 2011 Development of Solid Contact Micropipette Zn-Ion Selective Electrode for Corrosion Studies. *Anal. Lett.* **44**, 2876–2886. (doi:10.1080/00032719.2011.582545)
25. Kimmel, D. W., Leblanc, G., Meschievitz, M. E. & Cliffel, D. E. 2012 Electrochemical sensors and biosensors. *Anal. Chem.* **84**, 685–707. (doi:10.1021/ac202878q)
26. Bergner, S., Vatsyayan, P. & Matysik, F. 2013 Recent advances in high resolution scanning electrochemical microscopy of living cells--a review. *Anal. Chim. Acta* **775**, 1–13. (doi:10.1016/j.aca.2012.12.042)
27. Nioradze, N., Chen, R., Kim, J., Shen, M., Santhosh, P. & Amemiya, S. 2013 Origins of nanoscale damage to glass-sealed platinum electrodes with submicrometer and nanometer size. *Anal. Chem.* **85**, 6198–6202. (doi:10.1021/ac401316n)
28. Morris, C. A., Chen, C.-C. & Baker, L. A. 2012 Transport of redox probes through single pores measured by scanning electrochemical-scanning ion conductance microscopy (SECM-SICM). *Analyst* **137**, 2933–2938. (doi:10.1039/c2an16178h)
29. Comstock, D. J., Elam, J. W., Pellin, M. J. & Hersam, M. C. 2010 Integrated ultramicroelectrode-nanopipet probe for concurrent scanning electrochemical microscopy and scanning Ion conductance microscopy. *Anal. Chem.* **82**, 1270–1276. (doi:10.1021/ac902224q)
30. O'Connell, M. A. & Wain, A. J. 2014 Mapping electroactivity at individual catalytic nanostructures using high-resolution scanning electrochemical-scanning ion conductance microcopy. *Anal. Chem.* **86**, 12100–12107. (doi:10.1021/ac502946q)
31. Takahashi, Y., Shevchuk, A. I., Novak, P., Murakami, Y., Shiku, H., Korchev, Y. E. & Matsue, T. 2010 Simultaneous noncontact topography and electrochemical imaging by SECM/SICM featuring ion current feedback regulation. *J. Am. Chem. Soc.* **132**, 10118–10126. (doi:10.1021/ja1029478)
32. Takahashi, Y. et al. 2011 Multifunctional nanoprobes for nanoscale chemical imaging and localized chemical delivery at surfaces and interfaces. *Angew. Chemie - Int. Ed.* **50**, 9638–9642. (doi:10.1002/anie.201102796)
33. Macpherson, J. V. & Unwin, P. R. 2000 Combined scanning electrochemical-atomic force microscopy. *Anal. Chem.* **72**, 276–285. (doi:10.1021/ac990921w)

34. Kranz, C., Friedbacher, G., Mizaikofft, B., Lugstein, A., Smoliner, J. & Bertagnolli, E. 2001 Integrating an ultramicroelectrode in an AFM cantilever: Combined technology for enhanced information. *Anal. Chem.* **73**, 2491–2500. (doi:10.1021/ac001099v)
35. Kueng, A., Kranz, C., Lugstein, A., Bertagnolli, E. & Mizaikoff, B. 2003 Integrated AFM-SECM in tapping mode: Simultaneous topographical and electrochemical imaging of enzyme activity. *Angew. Chemie - Int. Ed.* **42**, 3238–3240. (doi:10.1002/anie.200351111)
36. Nellist, M. R. et al. 2017 Atomic force microscopy with nanoelectrode tips for high resolution electrochemical, nanoadhesion and nanoelectrical imaging. *Nanotechnology* **28**, 95711. (doi:10.1088/1361-6528/aa5839)
37. Ballesteros Katemann, B., Schulte, A. & Schuhmann, W. 2003 Constant-distance mode scanning electrochemical microscopy (SECM) - Part I: Adaptation of a non-optical shear-force-based positioning mode for SECM tips. *Chem. - A Eur. J.* **9**, 2025–2033. (doi:10.1002/chem.200204267)
38. McKelvey, K., Edwards, M. A., Unwin, P. R. & Kelvey, K. M. 2010 Intermittent Contact - Scanning Electrochemical Microscopy (IC - SECM): A New Approach for Tip Positioning and Simultaneous Imaging of Interfacial Topography and Activity. *Anal. Chem.* **82**, 6334–7. (doi:10.1021/ac101099e)
39. Momotenko, D., Page, A., Adobes-Vidal, M. & Unwin, P. R. 2016 Write-Read 3D Patterning with a Dual-Channel Nanopipette. *ACS Nano* **10**, 8871–8878. (doi:10.1021/acsnano.6b04761)
40. McKelvey, K., Kinnear, S. L., Perry, D., Momotenko, D. & Unwin, P. R. 2014 Surface Charge Mapping with a Nanopipette. *J. Am. Chem. Soc.* **136**, 13735–13744. (doi:10.1021/ja506139u)
41. Perry, D., Al Botros, R., Momotenko, D., Kinnear, S. L. & Unwin, P. R. 2015 Simultaneous Nanoscale Surface Charge and Topographical Mapping. *ACS Nano* **9**, 7266–7276. (doi:10.1021/acsnano.5b02095)
42. Perry, D., Paulose Nadappuram, B., Momotenko, D., Voyias, P. D., Page, A., Tripathi, G., Frenguelli, B. G. & Unwin, P. R. 2016 Surface Charge Visualization at Viable Living Cells. *J. Am. Chem. Soc.* **138**, 3152–3160. (doi:10.1021/jacs.5b13153)
43. Momotenko, D., McKelvey, K., Kang, M., Meloni, G. N. & Unwin, P. R. 2016 Simultaneous Interfacial Reactivity and Topography Mapping with Scanning Ion Conductance Microscopy (SICM). *Anal. Chem.* **88**, 2838–2846. (doi:10.1021/acs.analchem.5b04566)
44. Page, A., Perry, D., Young, P., Mitchell, D. A., Frenguelli, B. G. & Unwin, P. R. 2016 Fast Nanoscale Surface Charge Mapping with Pulsed-Potential Scanning Ion Conductance Microscopy. *Anal. Chem.* **88**, 10854–10859. (doi:10.1021/acs.analchem.6b03744)
45. Wei, C., Bard, A. J., Nagy, G. & Toth, K. 1995 Scanning Electrochemical Microscopy. 28. Ion-Selective Neutral Carrier-Based Microelectrode Potentiometry. *Anal. Chem.* **67**, 1346–1356. (doi:10.1021/ac00104a008)
46. Nitz, H., Kamp, J. & Fuchs, H. 1998 A combined scanning ion-conductance and shear-force microscope. *Probe Microsc.* **1**, 187–200.
47. Sa, N., Lan, W. J., Shi, W. & Baker, L. A. 2013 Rectification of ion current in nanopipettes by external substrates. *ACS Nano* **7**, 11272–11282. (doi:10.1021/nn4050485)
48. Korchev, Y. E., Gorelik, J., Lab, M. J., Sviderskaya, E. V, Johnston, C. L., Coombes, C. R., Vodyanoy, I. & Edwards, C. R. 2000 Cell volume

measurement using scanning ion conductance microscopy. *Biophys J* **78**, 451–457. (doi:10.1016/S0006-3495(00)76607-0)
49. Momotenko, D., Byers, J. C., McKelvey, K., Kang, M. & Unwin, P. R. 2015 High-Speed Electrochemical Imaging. *ACS Nano* **9**, 8942–8952. (doi:10.1021/acsnano.5b02792)
50. Novak, P. et al. 2009 Nanoscale live-cell imaging using hopping probe ion conductance microscopy. *Nat Meth* **6**, 279–281. (doi:10.1038/nmeth.1306)
51. Takahashi, Y., Murakami, Y., Nagamine, K., Shiku, H., Aoyagi, S., Yasukawa, T., Kanzaki, M. & Matsue, T. 2010 Topographic imaging of convoluted surface of live cells by scanning ion conductance microscopy in a standing approach mode. *Phys. Chem. Chem. Phys.* **12**, 10012–10017. (doi:10.1039/c002607g)
52. Yang, X., Liu, X., Zhang, X., Lu, H., Zhang, J. & Zhang, Y. 2011 Investigation of morphological and functional changes during neuronal differentiation of PC12 cells by combined Hopping Probe Ion Conductance Microscopy and patch-clamp technique. *Ultramicroscopy* **111**, 1417–1422. (doi:10.1016/j.ultramic.2011.05.008)
53. Chen, C.-C. & Baker, L. A. 2011 Effects of pipette modulation and imaging distances on ion currents measured with scanning ion conductance microscopy (SICM). *Analyst* **136**, 90–97. (doi:10.1039/c0an00604a)
54. Li, P., Liu, L., Yang, Y., Zhou, L., Wang, D., Wang, Y. & Li, G. 2015 Amplitude Modulation Mode of Scanning Ion Conductance Microscopy. *J. Lab. Autom.* **20**, 457–462. (doi:10.1177/2211068215573191)
55. Shevchuk, A. I., Gorelik, J., Harding, S. E., Lab, M. J., Klenerman, D. & Korchev, Y. E. 2001 Simultaneous measurement of Ca2+ and cellular dynamics: combined scanning ion conductance and optical microscopy to study contracting cardiac myocytes. *Biophys. J.* **81**, 1759–1764. (doi:10.1016/S0006-3495(01)75826-2)
56. Lipson, A. L., Ginder, R. S. & Hersam, M. C. 2011 Nanoscale in situ characterization of Li-ion battery electrochemistry via scanning ion conductance microscopy. *Adv. Mater.* **23**, 5613–5617. (doi:10.1002/adma.201103094)
57. Li, C., Johnson, N., Ostanin, V., Shevchuk, A., Ying, L., Korchev, Y. & Klenerman, D. 2008 High resolution imaging using scanning ion conductance microscopy with improved distance feedback control. *Prog. Nat. Sci.* **18**, 671–677. (doi:10.1016/j.pnsc.2008.01.011)
58. McKelvey, K., Perry, D., Byers, J. C., Colburn, A. W. & Unwin, P. R. 2014 Bias modulated scanning ion conductance microscopy. *Anal. Chem.* **86**, 3639–3646. (doi:10.1021/ac5003118)
59. Momotenko, D. & Girault, H. H. 2011 Scan-rate-dependent ion current rectification and rectification inversion in charged conical nanopores. *J. Am. Chem. Soc.* **133**, 14496–14499. (doi:10.1021/ja2048368)
60. Rheinlaender, J., Geisse, N. A., Proksch, R. & Schäffer, T. E. 2011 Comparison of scanning ion conductance microscopy with atomic force microscopy for cell imaging. *Langmuir* **27**, 697–704. (doi:10.1021/la103275y)
61. Korchev, Y. E., Milovanovic, M., Bashford, C. L., Bennett, D. C., Sviderskaya, E. V, Vodyanoy, I. & Lab, M. J. 1997 Specialized scanning ion-conductance microscope for imaging of living cells. *J. Microsc.* **188**, 17–23. (doi:10.1046/j.1365-2818.1997.2430801.x)
62. Happel, P., Hoffmann, G., Mann, S. A. & Dietzel, I. D. 2003 Monitoring cell

movements and volume changes with pulse-mode scanning ion conductance microscopy. *J. Microsc.* **212**, 144–151. (doi:10.1046/j.1365-2818.2003.01248.x)
63. Gorelik, J. et al. 2003 Dynamic assembly of surface structures in living cells. *Proc. Natl. Acad. Sci. U. S. A.* **100**, 5819–22. (doi:10.1073/pnas.1030502100)
64. Shin, W. & Gillis, K. D. 2006 Measurement of changes in membrane surface morphology associated with exocytosis using scanning ion conductance microscopy. *Biophys. J.* **91**, L63–L65. (doi:10.1529/biophysj.106.088559)
65. Lyon, A. R., MacLeod, K. T., Zhang, Y., Garcia, E., Kanda, G. K., Lab, M. J., Korchev, Y. E., Harding, S. E. & Gorelik, J. 2009 Loss of T-tubules and other changes to surface topography in ventricular myocytes from failing human and rat heart. *Proc. Natl. Acad. Sci. U. S. A.* **106**, 6854–6859. (doi:10.1073/pnas.0809777106)
66. Gorelik, J., Yang, L. Q., Zhang, Y., Lab, M., Korchev, Y. & Harding, S. E. 2006 A novel Z-groove index characterizing myocardial surface structure. *Cardiovasc. Res.* **72**, 422–429. (doi:10.1016/j.cardiores.2006.09.009)
67. Miragoli, M. et al. 2011 Scanning ion conductance microscopy: a convergent high-resolution technology for multi-parametric analysis of living cardiovascular cells. *J. R. Soc. Interface* **8**, 913–925. (doi:10.1098/rsif.2010.0597)
68. Zhang, S., Cho, S.-J., Busuttil, K., Wang, C., Besenbacher, F. & Dong, M. 2012 Scanning ion conductance microscopy studies of amyloid fibrils at nanoscale. *Nanoscale* **4**, 3105. (doi:10.1039/c2nr12049f)
69. Chen, C. C., Derylo, M. A. & Baker, L. A. 2009 Measurement of ion currents through porous membranes with scanning ion conductance microscopy. *Anal. Chem.* **81**, 4742–4751. (doi:10.1021/ac900065p)
70. Pastre, D., Iwamoto, H., Liu, J., Szabo, G. & Shao, Z. 2001 Characterization of AC mode scanning ion-conductance microscopy. *Ultramicroscopy* **90**, 13–19. (doi:10.1016/S0304-3991(01)00096-1)
71. Korchev, Y. E., Negulyaev, Y. a, Edwards, C. R., Vodyanoy, I. & Lab, M. J. 2000 Functional localization of single active ion channels on the surface of a living cell. *Nat. Cell Biol.* **2**, 616–619. (doi:10.1038/35023563)
72. Shi, W., Friedman, A. K. & Baker, L. A. 2016 Nanopore Sensing. *Anal. Chem.* **89**, 157–188. (doi:10.1021/acs.analchem.6b04260)
73. Chen, C. C., Zhou, Y. & Baker, L. A. 2011 Single-nanopore investigations with ion conductance microscopy. *ACS Nano* **5**, 8404–8411. (doi:10.1021/nn203205s)
74. Ivanov, A. P., Actis, P., Jönsson, P., Klenerman, D., Korchev, Y. & Edel, J. B. 2015 On-demand delivery of single DNA molecules using nanopipets. *ACS Nano* **9**, 3587–3595. (doi:10.1021/acsnano.5b00911)
75. Ying, L., Bruckbauer, A., Rothery, A. M., Korchev, Y. E. & Klenerman, D. 2002 Programmable delivery of DNA through a nanopipet. *Anal. Chem.* **74**, 1380–1385. (doi:10.1021/ac015674m)
76. Babakinejad, B. et al. 2013 Local delivery of molecules from a nanopipette for quantitative receptor mapping on live cells. *Anal. Chem.* **85**, 9333–9342. (doi:10.1021/ac4021769)
77. Shi, W., Sa, N., Thakar, R. & Baker, L. A. 2015 Nanopipette delivery: influence of surface charge. *Analyst* **140**, 4835–4842. (doi:10.1039/C4AN01073F)
78. Bruckbauer, A., Ying, L., Rothery, A. M., Zhou, D., Shevchuk, A. I., Abell, C.,

Korchev, Y. E. & Klenerman, D. 2002 Writing with DNA and Protein Using a Nanopipet for Controlled Delivery. *J. Am. Chem. Soc.* **124**, 8810–8811. (doi:http://dx.doi.org/10.1021/ja026816c)
79. Edwards, M. A., German, S. R., Dick, J. E., Bard, A. J. & White, H. S. 2015 High-Speed Multipass Coulter Counter with Ultrahigh Resolution. *ACS Nano* **9**, 12274–12282. (doi:10.1021/acsnano.5b05554)
80. McKelvey, K., Edwards, M. A. & White, H. S. 2016 Resistive Pulse Delivery of Single Nanoparticles to Electrochemical Interfaces. *J. Phys. Chem. Lett.* **7**, 3920–3924. (doi:10.1021/acs.jpclett.6b01873)
81. O'Connell, M. A., Snowden, M. E., McKelvey, K., Gayet, F., Shirley, I., Haddleton, D. M. & Unwin, P. R. 2014 Positionable vertical microfluidic cell based on electromigration in a theta pipet. *Langmuir* **30**, 10011–10018. (doi:10.1021/la5020412)
82. McKelvey, K., O'Connell, M. A. & Unwin, P. R. 2013 Meniscus confined fabrication of multidimensional conducting polymer nanostructures with scanning electrochemical cell microscopy (SECCM). *Chem. Comm.* **49**, 2986–2988. (doi:10.1039/c3cc00104k)
83. Actis, P., Maalouf, M. M., Kim, H. J., Lohith, A., Vilozny, B., Seger, R. A. & Pourmand, N. 2014 Compartmental genomics in living cells revealed by single-cell nanobiopsy. *ACS Nano* **8**, 546–553. (doi:10.1021/nn405097u)
84. Nashimoto, Y., Takahashi, Y., Zhou, Y., Ito, H., Ida, H., Ino, K., Matsue, T. & Shiku, H. 2016 Evaluation of mRNA Localization Using Double Barrel Scanning Ion Conductance Microscopy. *ACS Nano* **10**, 6915–6922. (doi:10.1021/acsnano.6b02753)
85. Sa, N. & Baker, L. A. 2011 Rectification of nanopores at surfaces. *J. Am. Chem. Soc.* **133**, 10398–10401. (doi:10.1021/ja203883q)
86. Edwards, M. A., Williams, C. G., Whitworth, A. L. & Unwin, P. R. 2009 Scanning Ion Conductance Microscopy : a Model for Experimentally Realistic Conditions and Image Interpretation. *Anal. Chem.* **81**, 4482–4492. (doi:10.1021/ac900376w)
87. Perry, D., Momotenko, D., Lazenby, R. A., Kang, M. & Unwin, P. R. 2016 Characterization of Nanopipettes. *Anal. Chem.* **88**, 5523–5530. (doi:10.1021/acs.analchem.6b01095)
88. Zhou, L., Zhou, Y. & Baker, L. A. 2014 Measuring Ions with Scanning Ion Conductance Microscopy. *Electrochem. Soc. Interface* **23**, 47–52.
89. Sa, N. & Baker, L. A. 2013 Experiment and Simulation of Ion Transport through Nanopipettes of Well-Defined Conical Geometry. *J. Electrochem. Soc.* **160**, H376–H381. (doi:10.1149/2.128306jes)
90. Wei, C., Bard, A. J. & Feldberg, S. W. 1997 Current Rectification at Quartz Nanopipet Electrodes. *Anal. Chem.* **69**, 4627–4633. (doi:10.1021/ac970551g)
91. Momotenko, D., Cortes-Salazar, F., Josserand, J., Liu, S., Shao, Y. & Girault, H. H. 2011 Ion current rectification and rectification inversion in conical nanopores : a perm-selective view. *Phys. Chem. Chem. Phys.* **13**, 5430–5440. (doi:10.1039/c0cp02595j)
92. Kinnear, S. L., Mckelvey, K., Snowden, M. E., Peruffo, M., Colburn, A. W. & Unwin, P. R. 2013 Dual-Barrel Conductance Micropipet as a New Approach to the Study of Local Interfacial Ionic Fluxes and Dissolution Processes. *Langmuir* **29**, 247143. (doi:10.1021/la403630u)
93. Perry, D., Parker, A. S., Page, A. & Unwin, P. R. 2016 Electrochemical Control of Calcium Carbonate Crystallization and Dissolution in Nanopipettes.

ChemElectroChem **3**, 2212–2220. (doi:10.1002/celc.201600547)
94. Adobes-Vidal, M., Maddar, F. M., Momotenko, D., Hughes, L. P., Wren, S. A. C., Poloni, L. N., Ward, M. D. & Unwin, P. R. 2016 Face-Discriminating Dissolution Kinetics of Furosemide Single Crystals: In Situ Three-Dimensional Multi-Microscopy and Modeling. *Cryst. Growth Des.* **16**, 4421–4429. (doi:10.1021/acs.cgd.6b00543)
95. Meng, L., Iacobini, J. G., Joseph, M. B., Macpherson, J. V & Newton, M. E. 2014 Laser heated boron doped diamond electrodes: effect of temperature on outer sphere electron transfer processes. *Faraday Discuss.* **172**, 421–38. (doi:10.1039/c4fd00044g)
96. Güell, A. G., Ebejer, N., Snowden, M. E., MacPherson, J. V. & Unwin, P. R. 2012 Structural correlations in heterogeneous electron transfer at monolayer and multilayer graphene electrodes. *J. Am. Chem. Soc.* **134**, 7258–7261. (doi:10.1021/ja3014902)
97. Rheinlaender, J., Schäffer, T. E., Rheinlaender, J. & Schäffer, T. E. 2009 Image formation, resolution, and height measurement in scanning ion conductance microscopy. *J. Appl. Phys.* **105**, 94905. (doi:10.1063/1.3122007)
98. Weber, A. E. & Baker, L. A. 2014 Experimental Studies of Resolution in Scanning Ion Conductance Microscopy. *J. Electrochem. Soc.* **161**, H924–H929. (doi:10.1149/2.0701414jes)
99. Shevchuk, A. I., Frolenkov, G. I., Sanchez, D., James, P. S., Freedman, N., Lab, M. J., Jones, R., Klenerman, D. & Korchev, Y. E. 2006 Imaging proteins in membranes of living cells by high-resolution scanning ion conductance microscopy. *Angew. Chemie - Int. Ed.* **45**, 2212–2216. (doi:10.1002/anie.200503915)
100. Thatenhorst, D., Rheinlaender, J., Schäffer, T. E., Dietzel, I. D. & Happel, P. 2014 Effect of Sample Slope on Image Formation in Scanning Ion Conductance Microscopy. *Anal. Chem.* **86**, 9838–9845. (doi:10.1021/ac5024414)
101. Klausen, L. H., Fuhs, T. & Dong, M. 2016 Mapping surface charge density of lipid bilayers by quantitative surface conductivity microscopy. *Nat. Commun.* **7**, 12447. (doi:10.1038/ncomms12447)
102. Haupt, A., Campetelli, A., Bonazzi, D., Piel, M., Chang, F. & Minc, N. 2014 Electrochemical Regulation of Budding Yeast Polarity. *PLoS Biol.* **12**. (doi:10.1371/journal.pbio.1002029)
103. Wong, J. Y., Langer, R. & Ingber, D. E. 1994 Electrically conducting polymers can noninvasively control the shape and growth of mammalian cells. *Proc. Natl. Acad. Sci. U. S. A.* **91**, 3201–3204. (doi:10.1073/pnas.91.8.3201)
104. Bakhti, M., Snaidero, N., Schneider, D., Aggarwal, S., Möbius, W., Janshoff, A., Eckhardt, M., Nave, K.-A. & Simons, M. 2013 Loss of electrostatic cell-surface repulsion mediates myelin membrane adhesion and compaction in the central nervous system. *Proc. Natl. Acad. Sci. U. S. A.* **110**, 3143–8. (doi:10.1073/pnas.1220104110)
105. van der Mei, H. C. & Busscher, H. J. 2012 Bacterial Cell Surface Heterogeneity: A Pathogen's Disguise. *PLoS Pathog.* **8**, 8–11. (doi:10.1371/journal.ppat.1002821)
106. Terada, A., Okuyama, K., Nishikawa, M., Tsuneda, S. & Hosomi, M. 2012 The effect of surface charge property on Escherichia coli initial adhesion and subsequent biofilm formation. *Biotechnol. Bioeng.* **109**, 1745–1754. (doi:10.1002/bit.24429)

107. Tedja, R., Lim, M., Amal, R. & Marquis, C. 2012 Effects of serum adsorption on cellular uptake profile and consequent impact of titanium dioxide nanoparticles on human lung cell lines. *ACS Nano* **6**, 4083–4093. (doi:10.1021/nn3004845)
108. Barisik, M., Atalay, S., Beskok, A. & Qian, S. 2014 Size Dependent Surface Charge Properties of Silica Nanoparticles. *J. Phys. Chem. C* **118**, 1836–1842. (doi:http://dx.doi.org/10.1021/jp410536n)
109. Kim, S. T., Saha, K., Kim, C. & Rotello, V. M. 2013 The role of surface functionality in determining nanoparticle cytotoxicity. *Acc. Chem. Res.* **46**, 681–691. (doi:10.1021/ar3000647)
110. Rivera-Gil, P. et al. 2013 The challenge to relate the physicochemical properties of colloidal nanoparticles to their cytotoxicity. *Acc. Chem. Res.* **46**, 743–749. (doi:10.1021/ar300039j)
111. Chung, T. H., Wu, S. H., Yao, M., Lu, C. W., Lin, Y. S., Hung, Y., Mou, C. Y., Chen, Y. C. & Huang, D. M. 2007 The effect of surface charge on the uptake and biological function of mesoporous silica nanoparticles in 3T3-L1 cells and human mesenchymal stem cells. *Biomaterials* **28**, 2959–2966. (doi:10.1016/j.biomaterials.2007.03.006)
112. Lee, K.-D., Hong, K. & Papahadjopoulos, D. 1992 Recognition of liposomes by cells: In vitro binding and endocytosis mediated by specific lipid headgroups and surface charge density. *Biochim. Biophys. Acta - Biomembr.* **1103**, 185–197. (doi:http://dx.doi.org/10.1016/0005-2736(92)90086-2)
113. Christianson, H. C., Svensson, K. J., van Kuppevelt, T. H., Li, J.-P. & Belting, M. 2013 Cancer cell exosomes depend on cell-surface heparan sulfate proteoglycans for their internalization and functional activity. *Proc. Natl. Acad. Sci. U. S. A.* **110**, 17380–5. (doi:10.1073/pnas.1304266110)
114. Shi, X. et al. 2013 Ca2+ regulates T-cell receptor activation by modulating the charge property of lipids. *Nature* **493**, 111–115. (doi:http://dx.doi.org/10.1038/nature11699)
115. Stumm, W. & Morgan, J. J. 1996 *Aquatic chemistry: chemical equilibria and rates in natural waters*. Third Edit. John Wiley & Sons. (doi:10.2307/2260132)
116. Schmickler, W. & Santos, E. 2010 *Interfacial Electrochemistry*. Second Edi. Springer Science & Business Media.
117. Behrens, S. H. & Grier, D. G. 2001 The charge of glass and silica surfaces. *J. Chem. Phys.* **115**, 6716–6721. (doi:10.1063/1.1404988)
118. Lan, W. J., Holden, D. A. & White, H. S. 2011 Pressure-dependent ion current rectification in conical-shaped glass nanopores. *J. Am. Chem. Soc.* **133**, 13300–13303. (doi:10.1021/ja205773a)
119. Siwy, Z., Heins, E., Harrell, C. C., Kohli, P. & Martin, C. R. 2004 Conical-nanotube ion-current rectifiers: The role of surface charge. *J. Am. Chem. Soc.* **126**, 10850–10851. (doi:10.1021/ja047675c)
120. White, H. S. & Bund, A. 2008 Ion current rectification at nanopores in glass membranes. *Langmuir* **24**, 2212–2218. (doi:10.1021/la702955k)
121. Rosentsvit, L., Wang, W., Schiffbauer, J., Chang, H. C. & Yossifon, G. 2015 Ion current rectification in funnel-shaped nanochannels: Hysteresis and inversion effects. *J. Chem. Phys.* **143**. (doi:10.1063/1.4936915)
122. Yin, X., Zhang, S., Dong, Y., Liu, S., Gu, J., Chen, Y., Zhang, X., Zhang, X. & Shao, Y. 2015 Ionic Current Rectification in Organic Solutions with Quartz Nanopipettes. *Anal. Chem.* **87**, 9070–9077. (doi:10.1021/acs.analchem.5b02337)

123. Clarke, R. W., Zhukov, A., Richards, O., Johnson, N., Ostanin, V. & Klenerman, D. 2013 Pipette-surface interaction: Current enhancement and intrinsic force. *J. Am. Chem. Soc.* **135**, 322–329. (doi:10.1021/ja3094586)
124. Feng, J., Liu, J., Wu, B. & Wang, G. 2010 Impedance Characteristics of Amine Modified Single Glass Nanopores. *Anal. Chem.* **82**, 4520–4528. (doi:10.1021/ac100440z)
125. Dzombak, D. A. & Morel, F. M. 1990 *Surface complexation modeling: hydrous ferric oxide*. John Wiley & Sons.
126. Unwin, P. R. & Bard, A. J. 1992 Scanning Electrochemical Microscopy. 14. Scanning Electrochemical Microscope Induced Desorption: A New Technique for the Measurement of Adsorption/Desorption Kinetics and Surface Diffusion Rates at the Solid/Liquid Interface. *J. Phys. Chem.* **5045**, 5035–5045. (doi:10.1021/j100191a055)
127. Davis, J., James, R. & Leckie, J. 1978 Surface Ionization and Complexation at the Oxide / Water Interface. *J. Colloid Interface Sci.* **63**, 480–499. (doi:10.1016/S0021-9797(78)80009-5)
128. Mclaughlin, S. 1989 The electrostatic properties of membranes. *Annu. Rev. Biophys. Biophys. Chem.* **18**, 113–136. (doi:10.1146/annurev.biophys.18.1.113)
129. Healy, T. W. & White, L. R. 1978 Ionizable surface group models of aqueous interfaces. *Adv. Colloid Interface Sci.* **9**, 303–345. (doi:10.1016/0001-8686(78)85002-7)
130. Kinraide, T. B. & Wang, P. 2010 The surface charge density of plant cell membranes (σ): An attempt to resolve conflicting values for intrinsic σ. *J. Exp. Bot.* **61**, 2507–2518. (doi:10.1093/jxb/erq082)
131. Henderson, D. & Boda, D. 2009 Insights from theory and simulation on the electrical double layer. *Phys. Chem. Chem. Phys.* **11**, 3822–30. (doi:10.1039/b815946g)
132. Rodolfa, K. T., Bruckbauer, A., Zhou, D., Korchev, Y. E. & Klenerman, D. 2005 Two-component graded deposition of biomolecules with a double-barreled nanopipette. *Angew. Chemie - Int. Ed.* **44**, 6854–6859. (doi:10.1002/anie.200502338)
133. Hirt, L. et al. 2015 Local surface modification via confined electrochemical deposition with FluidFM. *RSC Adv.* **5**, 84517–84522. (doi:10.1039/C5RA07239E)
134. Hirt, L., Ihle, S., Pan, Z., Dorwling-Carter, L., Reiser, A., Wheeler, J. M., Spolenak, R., Vörös, J. & Zambelli, T. 2016 Template-Free 3D Microprinting of Metals Using a Force-Controlled Nanopipette for Layer-by-Layer Electrodeposition. *Adv. Mater.* **28**, 2311–2315. (doi:10.1002/adma.201504967)
135. Chen, C. C., Zhou, Y., Morris, C. A., Hou, J. & Baker, L. A. 2013 Scanning ion conductance microscopy measurement of paracellular channel conductance in tight junctions. *Anal. Chem.* **85**, 3621–3628. (doi:10.1021/ac303441n)
136. Zhou, Y., Chen, C. C., Weber, A. E., Zhou, L. & Baker, L. A. 2014 Potentiometric-scanning ion conductance microscopy for measurement at tight junctions. *Tissue Barriers* **30**, 5669–5675. (doi:10.1021/la500911w)
137. Zhou, L., Zeng, Y., Baker, L. A. & Hou, J. 2015 A proposed route to independent measurements of tight junction conductance at discrete cell junctions. *Tissue Barriers* **8370**, 00–00. (doi:10.1080/21688370.2015.1105907)
138. Zhou, L., Zhou, Y., Shi, W. & Baker, L. a. 2015 Alternating Current Potentiometric Scanning Ion Conductance Microscopy (AC-PSICM). *J. Phys. Chem. C* , 150610134659006. (doi:10.1021/acs.jpcc.5b03120)

139. Shi, W., Zeng, Y., Zhou, L., Xiao, Y., Cummins, T. R. & Baker, L. A. 2016 Membrane patches as ion channel probes for scanning ion conductance microscopy. *Faraday Discuss.* **193**, 81–97. (doi:10.1039/c6fd00133e)
140. Nadappuram, B. P., McKelvey, K., Al Botros, R., Colburn, A. W. & Unwin, P. R. 2013 Fabrication and Characterization of Dual Function Nanoscale pH-Scanning Ion Conductance Microscopy (SICM) Probes for High Resolution pH Mapping. *Anal. Chem.* **85**, 8070–8074. (doi:10.1021/ac401883n)
141. Page, A., Kang, M., Armitstead, A., Perry, D. & Unwin, P. R. 2017 Quantitative Visualization of Molecular Delivery and Uptake at Living Cells with Self-Referencing Scanning Ion Conductance Microscopy (SICM) – Scanning Electrochemical Microscopy (SECM). *Anal. Chem.* , acs.analchem.6b04629. (doi:10.1021/acs.analchem.6b04629)
142. Morris, C. A., Chen, C.-C., Ito, T. & Baker, L. A. 2013 Local pH Measurement with Scanning Ion Conductance Microscopy. *J. Electrochem. Soc.* **160**, H430–H435. (doi:10.1149/2.028308jes)
143. Şen, M., Takahashi, Y., Matsumae, Y., Horiguchi, Y., Kumatani, A., Ino, K., Shiku, H. & Matsue, T. 2015 Improving the Electrochemical Imaging Sensitivity of Scanning Electrochemical Microscopy-Scanning Ion Conductance Microscopy by Using Electrochemical Pt Deposition. *Anal. Chem.* **87**, 3484–3489. (doi:10.1021/acs.analchem.5b00027)
144. Actis, P., Tokar, S. & Clausmeyer, J. 2014 Electrochemical nanoprobes for single-cell analysis. *ACS Nano* **8**, 875–84. (doi:10.1021/nn405612q)
145. O'Connell, M. A., Lewis, J. R. & Wain, A. J. 2015 Electrochemical imaging of hydrogen peroxide generation at individual gold nanoparticles. *Chem. Commun.* **51**, 10314–10317. (doi:10.1039/C5CC01640A)
146. Proksch, R., Lal, R., Hansma, P. K., Morse, D. & Stucky, G. 1996 Imaging the internal and external pore structure of membranes in fluid: TappingMode scanning ion conductance microscopy. *Biophys. J.* **71**, 2155–7. (doi:10.1016/S0006-3495(96)79416-X)
147. Pellegrino, M., Orsini, P. & De Gregorio, F. 2009 Use of scanning ion conductance microscopy to guide and redirect neuronal growth cones. *Neurosci. Res.* **64**, 290–296. (doi:10.1016/j.neures.2009.03.014)
148. Pellegrino, M., Orsini, P., Pellegrini, M., Baschieri, P., Dinelli, F., Petracchi, D., Tognoni, E. & Ascoli, C. 2012 Integrated SICM-AFM-optical microscope to measure forces due to hydrostatic pressure applied to a pipette. *Micro Nano Lett.* **7**, 317. (doi:10.1049/mnl.2011.0670)
149. Clarke, R. W., White, S. S., Zhou, D., Ying, L. & Klenerman, D. 2005 Trapping of proteins under physiological conditions in a nanopipette. *Angew. Chemie - Int. Ed.* **44**, 3747–3750. (doi:10.1002/anie.200500196)
150. Shevchuk, A. I., Hobson, P., Lab, M. J., Klenerman, D., Krauzewicz, N. & Korchev, Y. E. 2008 Endocytic pathways: Combined scanning ion conductance and surface confocal microscopy study. *Pflugers Arch. Eur. J. Physiol.* **456**, 227–235. (doi:10.1007/s00424-007-0410-4)
151. Shevchuk, A. I. et al. 2012 An alternative mechanism of clathrin-coated pit closure revealed by ion conductance microscopy. *J. Cell Biol.* **197**, 499–508. (doi:10.1083/jcb.201109130)
152. Bruckbauer, A., James, P., Zhou, D., Yoon, J. W., Excell, D., Korchev, Y., Jones, R. & Klenerman, D. 2007 Nanopipette delivery of individual molecules to cellular compartments for single-molecule fluorescence tracking. *Biophys. J.* **93**, 3120–3131. (doi:10.1529/biophysj.107.104737)

153. Rothery, A. M., Bruckbauer, A., Ying, L. M., Gorelik, J., Korchev, Y. E. & Klenerman, D. 2002 A novel light source for SNOM of living cells. *Biophys. J.* **82**, 497a–497a.
154. Snowden, M. E., Güell, A. G., Lai, S. C. S., McKelvey, K., Ebejer, N., O'Connell, M. a., Colburn, A. W. & Unwin, P. R. 2012 Scanning Electrochemical Cell Microscopy (SECCM): Theory and Experiment for Quan- titative High Resolution Spatially-Resolved Voltammetry and Simultaneous Ion- Conductance Measurements. *Anal. Chem.* **84**, 2483–2491. (doi:10.1021/ac203195h)
155. Ebejer, N., Güell, A. G., Lai, S. C. S., McKelvey, K., Snowden, M. E. & Unwin, P. R. 2013 Scanning electrochemical cell microscopy: a versatile technique for nanoscale electrochemistry and functional imaging. *Annu. Rev. Anal. Chem.* **6**, 329–51. (doi:10.1146/annurev-anchem-062012-092650)
156. Ebejer, N., Schnippering, M., Colburn, A. W., Edwards, M. A. & Unwin, P. R. 2010 Localized high resolution electrochemistry and multifunctional imaging: Scanning electrochemical cell microscopy. *Anal. Chem.* **82**, 9141–9145. (doi:10.1021/ac102191u)
157. Güell, A. G., Cuharuc, A. S., Kim, Y. R., Zhang, G., Tan, S. Y., Ebejer, N. & Unwin, P. R. 2015 Redox-Dependent spatially resolved electrochemistry at graphene and graphite step edges. *ACS Nano* **9**, 3558–3571. (doi:10.1021/acsnano.5b00550)
158. Güell, A. G., Meadows, K. E., Dudin, P. V., Ebejer, N., Macpherson, J. V. & Unwin, P. R. 2014 Mapping nanoscale electrochemistry of individual single-walled carbon nanotubes. *Nano Lett.* **14**, 220–224. (doi:10.1021/nl403752e)
159. Byers, J. C., Güell, A. G. & Unwin, P. R. 2014 Nanoscale electrocatalysis: Visualizing oxygen reduction at pristine, kinked, and oxidized sites on individual carbon nanotubes. *J. Am. Chem. Soc.* **136**, 11252–11255. (doi:10.1021/ja505708y)
160. Patten, H. V., Lai, S. C. S., MacPherson, J. V. & Unwin, P. R. 2012 Active sites for outer-sphere, inner-sphere, and complex multistage electrochemical reactions at polycrystalline boron-doped diamond electrodes (pBDD) revealed with scanning electrochemical cell microscopy (SECCM). *Anal. Chem.* **84**, 5427–5432. (doi:10.1021/ac3010555)
161. Chen, C., Jacobse, L., McKelvey, K., Lai, S. C. S., Koper, M. T. M. & Unwin, P. R. 2015 Voltammetric scanning electrochemical cell microscopy: dynamic imaging of hydrazine electro-oxidation on platinum electrodes. *Anal. Chem.* **87**, 5782–5789. (doi:10.1021/acs.analchem.5b00988)
162. Kang, M., Perry, D., Kim, Y. R., Colburn, A. W., Lazenby, R. A. & Unwin, P. R. 2015 Time-Resolved Detection and Analysis of Single Nanoparticle Electrocatalytic Impacts. *J. Am. Chem. Soc.* **137**, 10902–10905. (doi:10.1021/jacs.5b05856)
163. Lai, S., Lazenby, R. A., Kirkman, P. M. & Unwin, P. R. 2015 Nucleation, aggregative growth and detachment of metal nanoparticles during electrodeposition at electrode surfaces. *Chem. Sci.* **6**, 1126–1138. (doi:10.1039/C4SC02792B)
164. Unwin, P. R., Güell, A. G. & Zhang, G. 2016 Nanoscale Electrochemistry of sp 2 Carbon Materials: From Graphite and Graphene to Carbon Nanotubes. *Acc. Chem. Res.* **49**, 2041–2048. (doi:10.1021/acs.accounts.6b00301)
165. Oseland, E. E., Ayres, Z. J., Basile, A., Haddleton, D. M., Wilson, P. & Unwin, P. R. 2016 Surface patterning of polyacrylamide gel using scanning

electrochemical cell microscopy (SECCM). *Chem. Commun.* **52**, 9929–9932. (doi:10.1039/C6CC05153G)
166. Parker, A. S. et al. 2016 Combinatorial localized dissolution analysis: Application to acid-induced dissolution of dental enamel and the effect of surface treatments. *J. Colloid Interface Sci.* **476**, 94–102. (doi:10.1016/j.jcis.2016.05.018)
167. Nadappuram, P. B., McKelvey, K., Byers, J. C., Güell, A. G., Colburn, A. W., Lazenby, R. A. & Unwin, P. R. 2015 Quad-Barrel Multifunctional Electrochemical and Ion Conductance Probe for Voltammetric Analysis and Imaging. *Anal. Chem.* **87**, 3566–3573. (doi:10.1021/acs.analchem.5b00379)